

CHEMICAL ENGINEERING DIVISION

PHYSICAL CHEMISTRY OF LIQUID METALS

AND MOLTEN SALTS

SEMIANNUAL REPORT

January—June 1971

E. J. Cairns, F. A. Cafasso, P. T. Cunningham,
J. G. Eberhart, H. M. Feder, V. A. Maroni,
H. C. Schnyders, E. Veleckis,
A. D. Tevebaugh, and R. C. Vogel



U of C-ANL-USAEC

ARGONNE NATIONAL LABORATORY, ARGONNE, ILLINOIS

The facilities of Argonne National Laboratory are owned by the United States Government. Under the terms of a contract (W-31-109-Eng-38) between the U. S. Atomic Energy Commission, Argonne Universities Association and The University of Chicago, the University employs the staff and operates the Laboratory in accordance with policies and programs formulated, approved and reviewed by the Association.

MEMBERS OF ARGONNE UNIVERSITIES ASSOCIATION

The University of Arizona
Carnegie-Mellon University
Case Western Reserve University
The University of Chicago
University of Cincinnati
Illinois Institute of Technology
University of Illinois
Indiana University
Iowa State University
The University of Iowa

Kansas State University
The University of Kansas
Loyola University
Marquette University
Michigan State University
The University of Michigan
University of Minnesota
University of Missouri
Northwestern University
University of Notre Dame

The Ohio State University
Ohio University
The Pennsylvania State University
Purdue University
Saint Louis University
Southern Illinois University
The University of Texas at Austin
Washington University
Wayne State University
The University of Wisconsin

NOTICE

This report was prepared as an account of work sponsored by the United States Government. Neither the United States nor the United States Atomic Energy Commission, nor any of their employees, nor any of their contractors, subcontractors, or their employees, makes any warranty, express or implied, or assumes any legal liability or responsibility for the accuracy, completeness or usefulness of any information, apparatus, product or process disclosed, or represents that its use would not infringe privately-owned rights.

Printed in the United States of America
Available from
National Technical Information Service
U.S. Department of Commerce
5285 Port Royal Road
Springfield, Virginia 22151
Price: Printed Copy \$3.00; Microfiche \$0.95

ARGONNE NATIONAL LABORATORY
9700 South Cass Avenue
Argonne, Illinois 60439

CHEMICAL ENGINEERING DIVISION
PHYSICAL CHEMISTRY OF LIQUID METALS AND MOLTEN SALTS
SEMIANNUAL REPORT

January—June 1971

by

E. J. Cairns, F. A. Cafasso, P. T. Cunningham, J. G. Eberhart,
H. M. Feder, V. A. Maroni, H. C. Schnyders, E. Veleckis,
A. D. Tevebaugh, and R. C. Vogel

July 1971



TABLE OF CONTENTS

	<u>Page</u>
ABSTRACT.	1
SUMMARY	1
I. LIQUID METAL STUDIES	4
A. Thermodynamics	4
1. Phase Equilibria Studies of Binary Lithium-Chalcogen Systems.	4
a. Lithium-Sulfur System.	4
b. Lithium-Tellurium System	10
2. Lithium-Hydrogen-Metal Systems of Importance to Fusion Reactors.	12
a. Activity Measurements.	14
b. Phase Equilibria Studies	15
B. Theoretical Studies.	16
1. Noble Gas Solubilities in Liquid Metals.	16
2. Equation of State of Polarizable Soft-Sphere Fluids	19
II. MOLTEN SALT STUDIES.	29
A. Thermodynamics	29
1. Thermodynamics of Pseudo-Ternary Lithium Chalcogenide-Chalcogen-Alkali Halide Systems by Emf Methods	29
a. Selenium-Containing Systems.	29
b. Sulfur-Containing Systems.	37
2. Phase Diagram of the Pseudo-Ternary Lithium Selenide-Selenium-Alkali Halide System	39
B. Structure Investigations by Spectroscopic Methods.	41
1. Studies of Divalent Metal Halide Melts	43
2. Studies of Polyatomic Anions in the Molten State.	50
III. NUCLEATION STUDIES	55

LIST OF FIGURES

<u>No.</u>	<u>Title</u>	<u>Page</u>
I-1	Partial Phase Diagram of the Lithium-Sulfur System.	5
I-2	Schematic Diagram of Sample Cell and Furnace Assembly for Sulfur Vapor Pressure Determination	8
I-3	Plot of Calculated S_2 Partial Pressure and Measured Absorption Area as Function of Reciprocal Temperature	9
I-4	Partial Phase Diagram of Lithium-Tellurium System	11
I-5	Ostwald Coefficients of Noble Gases in Liquid Sodium.	18
I-6	Helmholtz Energy Cycle for Model Process of Condensation.	21
II-1	Schematic Diagram of Cell Used in Studying Effect of Alloy Composition on Emf for Selenium-Containing Systems.	30
II-2	Emf Measurements at 360°C as Function of Cathode Composition for Three Li/LiBr-RbBr/Li in Se Cells	32
II-3	Emf Measurements at 360°C as Function of Cathode Composition for Li/LiBr-RbBr/Li in Se Cell with $n_{Se}/(n_{Se} + n_E) = 0.903$	34
II-4	Li_2Se -Se-(LiBr-RbBr Eutectic) Pseudo-Ternary Phase Diagram.	35
II-5	Schematic Diagram of Cell Used in Studying Effect of Alloy Composition on Emf for Sulfur-Containing Systems.	38
II-6	Emf as Function of Temperature for Li/(42 at. % Li-Al) Alloy Couple.	40
II-7	Schematic Diagram of High-Temperature Centrifuge Assembly	42
II-8	Raman Spectrum of Molten $MgBr_2$ -KBr.	44
II-9	Raman Spectrum of Molten MgI_2 -KI.	45
II-10	Raman Spectra of $PbCl_2$ -KCl Melts.	49
II-11	Raman Spectra of $PbBr_2$ -KBr Melts.	51
II-12	Raman Spectrum of Molten $NaNH_2$ at 220°C with 5145 Å Exciting Radiation.	52

LIST OF FIGURES

<u>No.</u>	<u>Title</u>	<u>Page</u>
II-13	Raman Spectrum of Solid NaNH_2 at 25°C with 5145 \AA Exciting Radiation.	53
III-1	Relationship Between Mixture Parameter S and Surface Tension of Pure Components for Normal Alkane Mixtures at 20°C	57

LIST OF TABLES

<u>No.</u>	<u>Title</u>	<u>Page</u>
I-1	Results of Chemical Analysis of Quenched Lithium-Sulfur Samples.	7
I-2	Summary of Thermal Data for Lithium-Tellurium System	13
I-3	Atomic Parameters of Noble Gases	26
I-4	Dispersional Helmholtz Energies of Argon, Krypton, and Xenon.	27
II-1	Summary of Emf Data from $\text{Li/LiBr-RbBr (Eutectic)/Li}$ in Se Cells at 360°C	36
II-2	Observed and Calculated Frequencies for MgX_4^{2-} ($\text{X} = \text{Cl, Br, and I}$)	46
II-3	Force Constants and Bond Orders for MgX_4^{2-} ($\text{X} = \text{Cl, Br, and I}$)	47
II-4	Raman Data for Solid and Molten (220°C) NaNH_2	54

1957

1957

1957

1957

1957

1957

1957

1957

1957

1957

1957

1957

1957

CHEMICAL ENGINEERING DIVISION
PHYSICAL CHEMISTRY OF LIQUID METALS AND MOLTEN SALTS
SEMIANNUAL REPORT

January-June 1971

by

E. J. Cairns, F. A. Cafasso, P. T. Cunningham, J. G. Eberhart,
H. M. Feder, V. A. Maroni, H. C. Schnyders, E. Veleckis,
A. D. Tevebaugh, and R. C. Vogel

ABSTRACT

The thermodynamic and chemical properties of liquid metals and molten salts continue to be of interest. Partial phase diagrams for the lithium-sulfur and lithium-tellurium systems are reported. Pseudo-ternary systems of the type lithium chalcogenide-chalcogen-alkali halide eutectic have been studied by several techniques, including emf measurement, and thermodynamic and phase data are reported. Refinements in a model for calculating the solubility of noble gases in liquid metals have been made. Raman spectroscopy has been used to study the structure of divalent metal halides and polyatomic anions in melts. Preliminary studies of lithium-hydrogen-metal systems of importance to fusion reactors are reported. A study of the homogeneous nucleation of vapor bubbles in superheated liquids has been started.

SUMMARY

Liquid Metal Studies

Thermodynamics of Liquid Metals. Phase equilibria in the lithium-sulfur and lithium-tellurium systems are being studied. In the lithium-sulfur system, the only intermediate phase found is Li_2S , which melts near 1372°C . A miscibility gap extends from less than 0.5 to 36.8 at.% lithium at the monotectic temperature of 365°C . The extent of the gap does not appear to have changed at 508°C . Two intermediate phases are found in the lithium-tellurium system: Li_2Te (mp $>825^\circ\text{C}$) and LiTe_3 (mp $\sim 459^\circ\text{C}$). The eutectic between LiTe_3 and tellurium (mp 449.8°C) occurs at $\sim 423^\circ\text{C}$ whereas that between Li_2Te and LiTe_3 occurs at $\sim 448^\circ\text{C}$.

Lithium-Hydrogen-Metal Systems of Importance to Fusion Reactors. Liquid lithium appears to be uniquely suited to act as the blanket material in present conceptual designs for deuterium-tritium fueled fusion reactors. Because much of the thermodynamic information on the lithium-hydrogen, -deuterium, and -tritium systems is fragmentary, particularly for conditions that are projected for fusion reactors, we have initiated a program to study chemical activities and phase equilibria in these systems. The results of these studies are expected to provide useful information for the design of thermonuclear reactor fuel cycling and recovery

processes and to add to our understanding of solutions of hydrogen in liquid metals.

Theoretical Studies. Theoretical studies of the solubility of gases in liquid metals have continued. A dilute solution of a noble-gas element in a liquid metal can be considered as an "alloy" which is sufficiently simple in nature to permit calculation of its thermodynamic properties from its idealized model. The solubilities of helium, argon, krypton, and xenon in liquid sodium, so calculated, are in reasonable agreement with experimental values and point the way toward further refinements. In particular, when the model calculation is applied to liquified argon, krypton, and xenon, the calculated dispersion energies fall short of the experimental ones by 5 to 15%, showing the need for the inclusion of multipolar and vibrational effects.

Molten Salt Studies

Thermodynamics. EMF measurements on Li/LiBr-RbBr/Li in Se cells have been interpreted in terms of a pseudo-ternary phase equilibrium involving selenium, electrolyte, and cell reaction products (Li_2Se). Interpretation as a simple binary system has been precluded by the significant mutual solubilities of the ternary components. Phase boundaries within the pseudo-ternary system at 360°C have been located by emf measurements. The system contains an interesting region of three-liquid immiscibility. Thermodynamic data have also been obtained. Similar studies for sulfur-containing systems are planned.

In order to complete the determination of the Se-(LiBr-RbBr eutectic)- Li_2Se pseudo-ternary system, phase equilibrium studies are in progress to investigate the compositions of phases at 360°C . Equilibrium phases at various compositions are separated by high-temperature centrifugation and analyzed both chemically and microscopically. The locations of the corners of the three-liquid region have been determined and measurements of the other phases are in progress.

Structure Investigations by Spectroscopic Methods. Raman spectroscopic studies have demonstrated the existence of complex equilibria in Mg(II) - and Pb(II) -halide systems, and in some cases the structures of the predominant complexes have been elucidated. The existence of the tetrahedral complexes MgCl_4^{2-} , MgBr_4^{2-} , and MgI_4^{2-} has been confirmed both spectroscopically and by normal-coordinate analyses. The structure of the NaNH_2 has been examined in the solid and in the molten states. The NH_2^{1-} ion was found to be bent in both phases, and there was evidence of some form of phase transition between 25°C and the melting point (204°C).

Nucleation Studies

A study has been initiated of the homogeneous nucleation of vapor bubbles in superheated liquids. Initial experiments will be performed on binary mixtures of normal alkanes to test recent theories on nucleation in liquid mixtures. A key parameter in the theoretical expressions is surface tension. Since experimental surface-tension data for alkanes at

elevated temperatures are not presently available, techniques are being sought to estimate these values. An empirical relation that fits the available surface-tension experimental data has been found.

I. LIQUID METAL STUDIES
(E. J. Cairns, F. A. Cafasso)

A. Thermodynamics

The Chemical Engineering Division has been carrying out research on liquid metals, including both the theoretical and experimental aspects of several areas of importance to the Atomic Energy Commission. These investigations have dealt with (1) the behavior of liquid sodium (as a coolant in nuclear reactors) and other alkali metals, (2) the thermodynamic and electrochemical properties of electrochemical cells with liquid alkali metals as anodes and liquid heavy metals or liquid chalcogens as cathodes, and (3) phase diagrams of importance to these studies. Recently, the study of lithium interactions with hydrogen isotopes--especially in those respects which relate to fusion power--has been added to the program. Investigations have begun on the determination of the activities of hydrogen isotopes in lithium as a function of hydrogen partial pressure (or concentration), and on the interactions among lithium, hydrogen, and the refractory metals that might be used in fusion-reactor walls.

1. Phase Equilibrium Studies of Binary Lithium-Chalcogen Systems
(P. T. Cunningham, S. A. Johnson)

a. Lithium-Sulfur System

Preliminary thermal data on the lithium-sulfur system have been previously reported.¹ Those data identify the thermal invariants of the system which provide the basic form of the phase diagram as indicated in Fig. I-1. Recent work has been directed toward determining the extent of the miscibility gap, which exists on the sulfur-rich side of Li_2S above 365°C , and the location of the upper liquidus separating liquid 2 (L_2) and solid Li_2S .

Previous efforts to determine the extent of the miscibility gap by chemical analysis of quenched samples were frustrated by failure of the two phases to separate completely under normal gravity. This difficulty was overcome by use of the high-temperature centrifuge described in Section II.A.2 of this report. Sample mixtures having an overall composition near the center of the miscibility gap (about 18 at.% lithium in sulfur) were prepared by mixing 97+ pure Li_2S (supplied by the Foote Mineral Company, Exton, Pennsylvania) with 99.999% pure sulfur (supplied by the American Smelting and Refining Company, South Plainfield, New Jersey). The samples, each weighing about 0.5 g, were placed in quartz ampuls which were evacuated, sealed, and placed in a rocking furnace where they were mixed for two days at 440°C . The ampuls were then loaded into the centrifuge where they were heated to about 25°C above the centrifugation temperature for twelve hours, followed by centrifugation at 1800 rpm (250 g) for 6 to 7 hr prior to quenching in liquid nitrogen.

¹ Chemical Engineering Division Annual Report--1970, USAEC report ANL-7775, Section V.A.1.a(2) (in press).

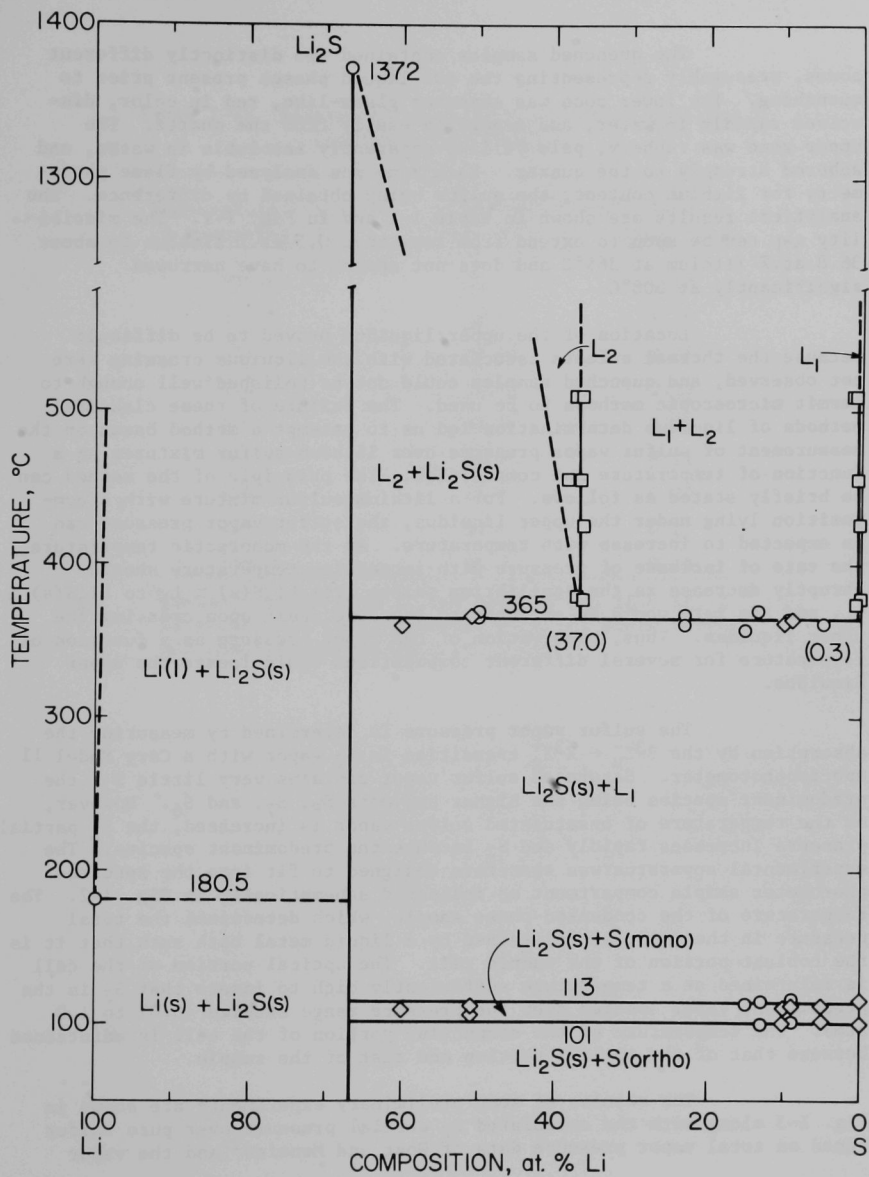


Fig. I-1. Partial Phase Diagram of the Lithium-Sulfur System

□ Chemical Analysis Data

○ Heating and Cooling Curve Data

◇ Differential Thermal Analysis Data

The quenched samples contained two distinctly different zones, presumably representing the two liquid phases present prior to quenching. The lower zone was somewhat glass-like, red in color, dissolved rapidly in water, and separated easily from the quartz. The upper zone was rubbery, pale yellow, apparently insoluble in water, and adhered strongly to the quartz. Each zone was analyzed by flame photometry for lithium content, the sulfur being obtained by difference. The analytical results are shown in Table I-1 and in Fig. I-1. The miscibility gap can be seen to extend from less than 0.5 at.% lithium to about 36.8 at.% lithium at 365°C and does not appear to have narrowed significantly at 508°C.

Location of the upper liquidus proved to be difficult because the thermal effects associated with the liquidus crossing were not observed, and quenched samples could not be polished well enough to permit microscopic methods to be used. The failure of these classical methods of liquidus determination led us to attempt a method based on the measurement of sulfur vapor pressure over lithium-sulfur mixtures as a function of temperature and composition. The principle of the method can be briefly stated as follows. For a lithium-sulfur mixture with a composition lying under the upper liquidus, the sulfur vapor pressure can be expected to increase with temperature. At the monotectic temperature, the rate of increase of pressure with increasing temperature should abruptly decrease as the equilibrium shifts from $\text{Li}_2\text{S(s)} \rightleftharpoons \text{L}_1$ to $\text{Li}_2\text{S(s)} \rightleftharpoons \text{L}_2$, and the rate would be expected to increase again upon crossing the upper liquidus. Thus, observation of the vapor pressure as a function of temperature for several different compositions would locate the upper liquidus.

The sulfur vapor pressure is determined by measuring the absorption by the $\text{B}^3\Sigma_u^- \leftarrow \text{X}^3\Sigma_g^-$ transition in S_2 vapor with a Cary Model 11 spectrophotometer. Saturated sulfur vapor contains very little S_2 , the predominant species being the higher polymers S_8 , S_7 , and S_6 . However, as the temperature of unsaturated sulfur vapor is increased, the S_2 partial pressure increases rapidly and S_2 becomes the predominant species. The experimental apparatus was therefore designed to fit into the spectrophotometer sample compartment as indicated schematically in Fig. I-2. The temperature of the condensed-phase sample, which determines the total pressure in the cell, is maintained by a liquid metal bath such that it is the coolest portion of the sample cell. The optical portion of the cell is maintained at a temperature sufficiently high to insure that S_2 is the predominant vapor species over the pressure range studied (0.01 to 1.0 atm). The temperature of the connecting portion of the cell is maintained between that of the optical portion and that of the sample.

The results of some preliminary experiments are shown in Fig. I-3 along with the calculated S_2 partial pressure over pure sulfur based on total vapor pressure data of West and Menzies² and the vapor

² W. A. West and A. W. C. Menzies, J. Phys. Chem. 33, 1880 (1929).

Table I-1. Results of Chemical Analysis of Quenched Lithium-Sulfur Samples

Temperature Prior to Quenching, °C	Composition, at. % Li ^a	
	Lower Zone	Upper Zone
375.0	36.6	0.62
375.0	36.7	0.79
377.0	37.0*	0.34*
416.5	36.8	0.32
416.5	36.0	0.31
456.0	36.8	0.21
456.0	38.5	0.20
508.0	37.1	0.17
508.0	36.7	0.15

^aOverall composition of the samples was 18.0 at. % Li except for samples marked with (*) where overall composition was 15.2 at. % Li.

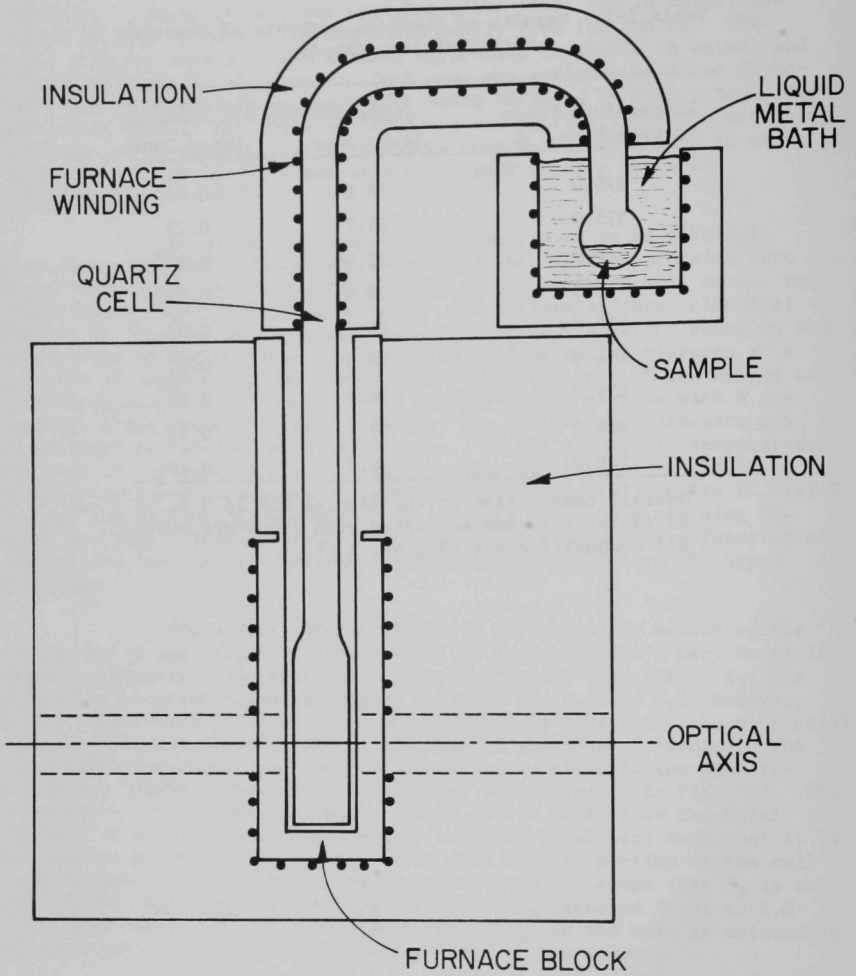


Fig. I-2. Schematic Diagram of Sample Cell and Furnace Assembly for Sulfur Vapor Pressure Determination

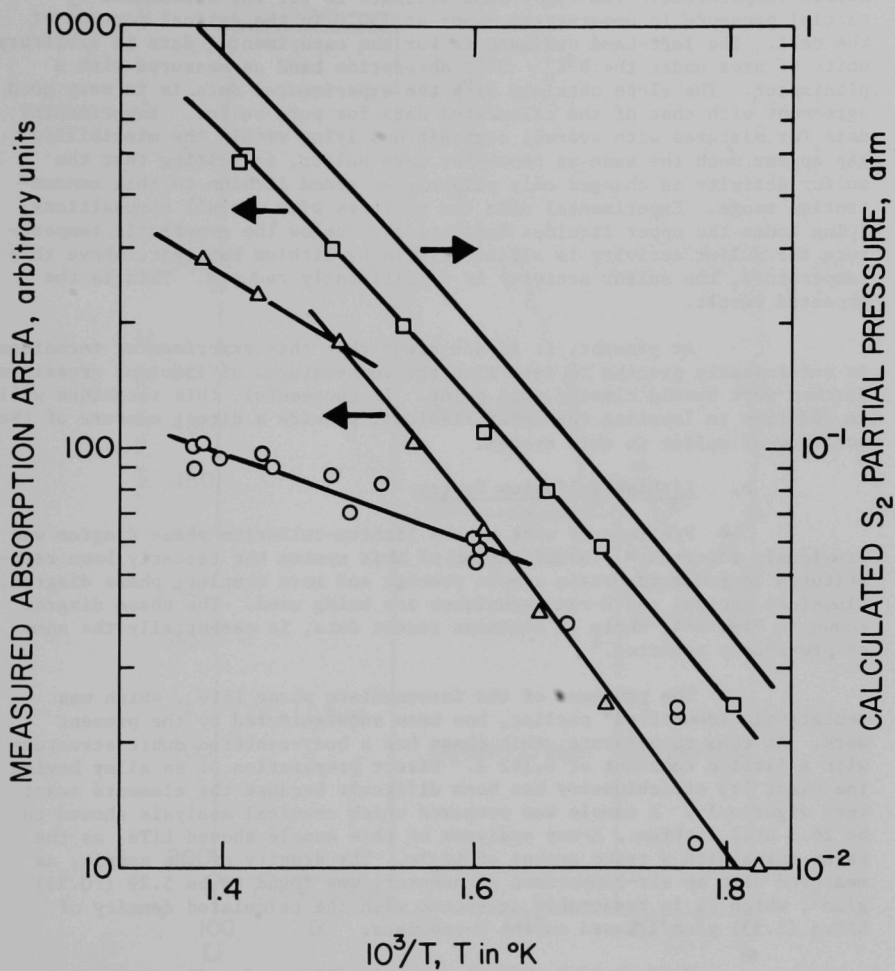


Fig. I-3. Plot of Calculated S_2 Partial Pressure and Measured Absorption Area as Function of Reciprocal Temperature

phase equilibrium constants of Detry et al.³ The abscissa is reciprocal sample temperature. The right-hand ordinate is for the calculated S_2 partial pressure in unsaturated vapor at 750°C in the optical portion of the cell. The left-hand ordinate is for the experimental data in arbitrary units of area under the $B_{2u}^{3-} + X_{2g}^{3-}$ absorption band as measured with a planimeter. The slope obtained with the experimental data is in very good agreement with that of the calculated data for pure sulfur. Experimental data for mixtures with overall compositions lying within the miscibility gap appear much the same as those for pure sulfur, indicating that the sulfur activity is changed only slightly by added lithium in this concentration range. Experimental data for mixtures with overall compositions lying under the upper liquidus indicate that below the monotectic temperature the sulfur activity is altered little by lithium but that, above this temperature, the sulfur activity is significantly reduced. This is the expected result.

At present, it is not clear that this experimental technique is sufficiently precise to determine the temperatures of liquidus crossings. Further work should clarify this point. If successful, this technique will, in addition to locating the upper liquidus, provide a direct measure of the activity of sulfur in this system.

b. Lithium-Tellurium System

Preliminary work on the lithium-tellurium phase diagram was previously reported.⁴ Investigation of this system has recently been reinstituted in order to obtain a more precise and more complete phase diagram. Classical thermal and X-ray techniques are being used. The phase diagram shown in Fig. I-4, while it contains recent data, is essentially the same as previously reported.⁴

The presence of the intermediate phase $LiTe_3$, which was tentatively identified⁴ earlier, has been substantiated by the present work. At room temperature, this phase has a body-centered cubic structure with a lattice constant of 6.162 Å. Direct preparation of an alloy having the exact 1:3 stoichiometry has been difficult because the elements react very vigorously. A sample was prepared which chemical analysis showed to be 26.3 at.% lithium. X-ray analyses of this sample showed $LiTe_3$ as the major phase with a trace amount of Li_2Te . The density of the sample, as measured with an air-comparison pycnometer, was found to be 5.29 (± 0.25) g/cm³, which is in reasonable agreement with the calculated density of $LiTe_3$ (5.531 g/cm³) based on the X-ray data.

Differential thermal analysis (DTA) and ordinary heating and cooling curves were used to determine the thermal effects of the

³ D. Detry, J. Drowart, P. Goldfinger, H. Keller, and H. Rickert, Z. Phys. Chem. (Leipzig) Neue Folge 55, 314 (1967).

⁴ Chemical Engineering Division Semiannual Report--1968, USAEC report ANL-7575, pp. 140-142 (1969).

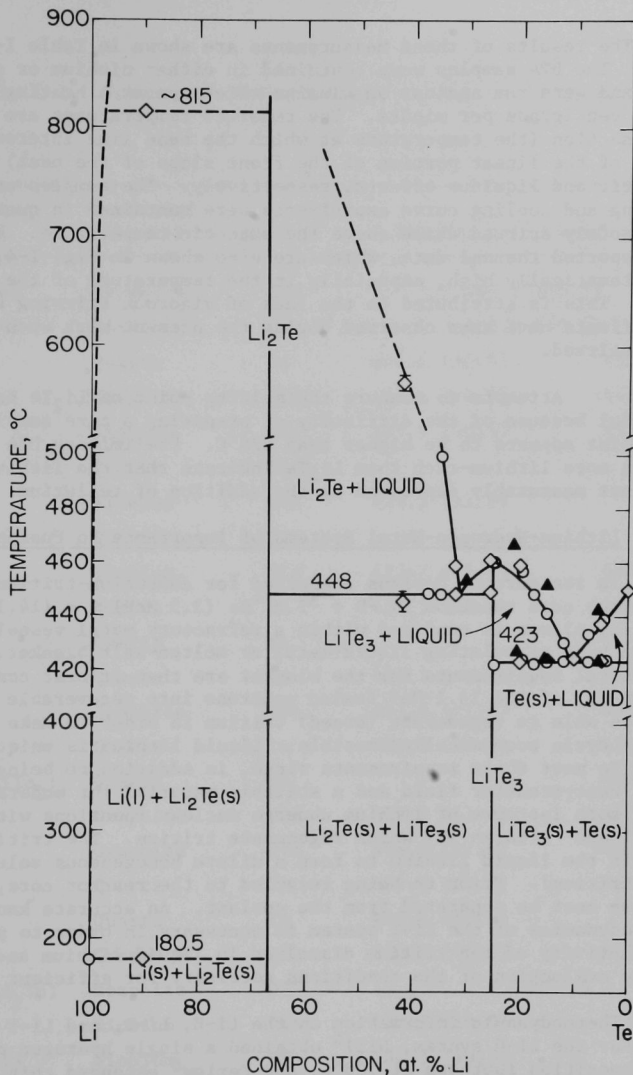


Fig. I-4. Partial Phase Diagram of Lithium-Tellurium System

- △ Heating and Cooling Curve Data (Previous Work, See Ref. 4)
- Heating and Cooling Curve Data (Present Work)
- Differential Thermal Analysis Data (Present Work)

system. The results of these measurements are shown in Table I-2 and Fig. I-4. The DTA samples were contained in either niobium or graphite capsules and were run against an alumina reference at a heating rate of 5 degrees centigrade per minute. The reported temperatures are those of the intersection (the temperature at which the base line intersects an extension of the linear portion of the front slope of the peak) and peak for eutectic and liquidus effects, respectively. The samples used in the heating and cooling curve experiments were contained in quartz and were vigorously stirred while above the eutectic temperature. The previously reported thermal data, which are also shown in Fig. I-4, appear to be systematically high, especially in the temperature of the liquidus crossing. This is attributed to the lack of vigorous stirring since similar effects have been observed during the present work when the samples were not stirred.

Attempts to measure the melting point of Li_2Te have been unsuccessful because of the difficulty of preparing a pure sample. The melting point appears to be higher than 825°C . Preliminary DTA results on samples more lithium-rich than Li_2Te indicate that the lithium melting point is not measurably depressed by the addition of tellurium.

2. Lithium-Hydrogen-Metal Systems of Importance to Fusion Reactors

In the current designs conceived for deuterium-tritium fusion reactors [the core reaction is $^2\text{D} + ^3\text{T} \rightarrow ^4\text{He} (3.5 \text{ MeV}) + \text{n} (14.1 \text{ MeV})$], the reacting plasma is confined within a refractory metal vessel which is surrounded by a circulating liquid-metal or molten-salt blanket. The basic physical requirements for the blanket are that it must convert the kinetic energy of the 14.1-MeV fusion neutrons into recoverable heat and be able to regenerate (breed) tritium in order to make a tritium-based fuel cycle economically feasible. Liquid lithium is uniquely qualified to meet these requirements since, in addition to being an excellent heat-transfer fluid and a suitable material for moderating fast neutrons, both isotopes of lithium undergo nuclear reactions with neutrons [$^6\text{Li}(\text{n}, \alpha)\text{T}$ and $^7\text{Li}(\text{n}, \text{n}')\text{T}$] which regenerate tritium. The tritium will dissolve in the liquid lithium to form a dilute homogeneous solution (~ 10 ppm tritium). Prior to being recycled to the reactor core, most of the tritium must be separated from the coolant. An accurate knowledge of the thermodynamics of the Li-T system is necessary in order to predict the chemical activity of the tritium dissolved in liquid lithium and to make a reasonable evaluation of the conditions necessary for efficient separation.

Thermodynamic information on the Li-H, Li-D, and Li-T systems is sparse. For the Li-H system, Hill⁵ obtained a single hydrogen pressure versus composition isotherm at 700°C , and Perlow⁶ extended this work by

⁵ L. L. Hill, Ph.D. dissertation, University of Chicago (1938).

⁶ M. R. J. Perlow, Ph.D. dissertation, University of Chicago (1941).

Table I-2. Summary of Thermal Data for Lithium-Tellurium System

Composition, at.% Li	Container Material	Method ^a	Thermal Effects Noted, ^b °C	
0.0 (Te)	Graphite	DTA	449.7 (±0.5)	
0.0 (Te)	Niobium	DTA	450.0 (±0.5)	
4.1	Quartz	TA	423.6 (±0.5)	439.0 (±0.5)
5.0	Graphite	DTA	423.8 (±0.5)	<440.0
5.0	Niobium	DTA	423.9 (±0.5)	437.4 (±3.0)
7.4	Quartz	TA		
10.0	Niobium	DTA	424.2 (±1.0)	--
11.9	Quartz	TA		
15.0	Niobium	DTA	423.7 (±1.0)	460.0 (±4.0)
15.1	Quartz	TA	422.7 (±0.5)	441.5 (±1.0)
17.5	Quartz	TA		
19.7	Quartz	TA	423.3 (±0.5)	457.0 (±2.0)
20.0	Graphite	DTA	423.0 (±1.0)	459.0 (±1.0)
~25.0	Quartz	TA	422.4 (±2.0)	459.2 (±0.5)
25.0 (LiTe ₃)	Quartz	TA	--	459.0 (±0.5)
~25.0	Graphite	DTA	449.0 (±1.0)	461.0 (±2.0)
32.1	Graphite	DTA	448.0 (±1.0)	<460.0
34.9	Quartz	TA	449.0 (±1.0)	499.4 (±2.0)
37.2	Quartz	TA	448.6 (±0.5)	--
42.0	Graphite	DTA	446.0 (±4.0)	~470.0
66.7 (Li ₂ Te)	Graphite	DTA	>825.0	
90.0	Niobium	DTA	180.5 (±0.5)	815 (±10)
100.0 (Li)	Niobium	DTA	180.5 (±0.5)	

^a DTA--differential thermal analysis; TA--heating or cooling curves.

^b The lower temperatures are presumed to be those of eutectic reactions and correspond to the intersection temperature for DTA and thermal arrests in heating or cooling curves. The higher temperatures are presumed to be liquidus crossings and correspond to peak temperature for DTA and thermal breaks in heating or cooling curves.

obtaining isothermal data at 770°C and 825°C. More recently, Heumann and Salmon⁷ remeasured the 700°C isotherm. The large scatter of these data and the insufficient number of isotherms make it difficult to extract meaningful thermodynamic information, particularly in the dilute-solution regions where current interest is centered. Heumann and Salmon also measured the dissociation pressures in the Li-LiD and Li-LiT systems as functions of composition at 700, 750, and 800°C. Here again the results are fragmentary and not readily amenable to the extraction of useful thermodynamic information for the conditions that will obtain in a fusion reactor.

In view of the paucity of data associated with the tritium inventory problems in the fusion-reactor blankets, we have initiated studies to obtain more comprehensive and reliable pressure-composition-temperature data for the systems Li-LiH, Li-LiD, and Li-LiT. The initial stages of these studies will be focused on the determination of (1) the activity of hydrogen (and later deuterium and tritium) in solutions in liquid lithium over the temperature range 600 to 1000°C, and (2) phase boundaries and interactions in lithium-hydrogen-refractory metal systems. In later stages of the study, methods will be sought for a quantitative separation of hydrogen from lithium, probably utilizing electrochemical techniques for promoting hydrogen transfer through thin metallic membranes.

a. Activity Measurements (E. Veleckis, E. Van Deventer)

Hydrogen-activity measurements will be made using a tensi-metric technique. A special apparatus (Sieverts' apparatus) has been constructed for the volumetric measurement and transfer of hydrogen. With this apparatus, small, measured amounts of hydrogen can be consecutively added to a reaction tube containing the lithium sample. Equilibrium hydrogen pressures measured after each successive addition of hydrogen to a known amount of lithium will provide a set of pressure-composition isotherms from which the requisite thermodynamic data can be obtained. The data will be correlated with existing theoretical treatments of solutions of hydrogen in liquid metals.

The high-purity lithium to be used for activity measurements will be sealed in reaction tubes made of Armco iron. Meacham, Hill, and Gordus⁸ recently demonstrated that, for the Na-H system, a crucible that is only partially filled with sodium can lead to erroneous results due to nonequilibrium conditions created by the formation of a solid hydride either on the sodium surface or in the vapor space. They minimized this problem by eliminating gas bubbles during the sealing of the capsule. In the present study we intend to apply this method to seal lithium in thin-walled iron tubes. The thermal expansion of lithium in the fully filled tubes will be accommodated by flattening the middle portions of the tubes

⁷ F. K. Heumann and O. N. Salmon, The Lithium Hydride, Deuteride, and Tritide Systems, USAEC report KAPL-1667 (1956).

⁸ S. A. Meacham, E. F. Hill, and A. A. Gordus, The Solubility of Hydrogen in Sodium, APDA-241, Atomic Power Development Associates (1970).

to an elliptical cross section prior to their being filled with lithium. A small correction will have to be applied to the results to take into account the known⁹ solubility of hydrogen in iron. Iron was selected because of its corrosion resistance toward lithium,¹⁰ low hydrogen solubility, and the rapid diffusion of hydrogen in iron.¹¹

b. Phase Equilibria Studies (V. A. Maroni, E. J. Hathaway)

Experiments have been initiated to study phase equilibria and other interactions in lithium-hydrogen-refractory metal systems. The results of these studies will be combined with data from the hydrogen-activity measurements to determine phase diagrams and other important thermodynamic properties for these systems.

Most of the experimental work involved in the phase-diagram determinations will be carried out using conventional thermal analysis and differential thermal analysis (DTA) techniques. The general method will parallel that used by Messer et al.¹² to study portions of the lithium-lithium hydride binary system. In a typical experiment, a sample of lithium is sealed into an iron container, the iron container is placed in a specially designed thermal analysis bomb, and the bomb is connected to a hydrogen-transfer system (Sieverts' line). Incremental amounts of hydrogen are added to the bomb and allowed to react with the lithium. (The hydrogen reaches the lithium by diffusing through the walls of the iron container.) After each hydrogen addition, the partial pressure is allowed to reach equilibrium, and cooling curves are recorded at constant pressure. The composition at each thermal-arrest temperature is determined from the equilibrium pressure using the results of the tensimetric studies described in the previous section. These temperatures and compositions are then used to construct the lithium-hydrogen phase diagram. In subsequent experiments, the effects (if any) of the presence of various refractory metals and alloys on the phase boundaries will be determined.

The Sieverts' vacuum system needed for these experiments has been constructed. A manostat has been designed and is partially constructed. Construction of the manostat and the thermal analysis bomb and testing of the entire system remain to be completed before the thermal analysis experiments can begin.

⁹ P. D. Blake, M. F. Jordan, and W. I. Pumphrey, Iron and Steel Institute, Spec. Rept. 73, p. 76 (1962).

¹⁰ M. F. Amateau, The Effect of Molten Alkali Metals on Containment Metals and Alloys at High Temperatures, DMIC-169, Defense Metals Information Center (1962).

¹¹ R. W. Webb, Hydrogen Permeation Through Metals, NAA-SR-TDR-9844, Atomics International (1964).

¹² C. E. Messer, E. B. Daman, P. C. Maybury, J. Mellor, and R. A. Seales, J. Phys. Chem. 62, 220 (1958).

B. Theoretical Studies (H. Schnyders, H. M. Feder)

1. Noble Gas Solubilities in Liquid Metals

The behavior of liquid metals as solvents is in many respects quite unlike that of normal insulating liquids. As a first step toward understanding the liquid-metal solvent problem, we have chosen to study noble-gas solutes. Since we can, with reasonable certainty, assert that there are no bound states for the conduction electrons at the site of the solute molecule, nor donation of electrons to the conduction band, this simplification allows us to ignore the charge-transfer effects which occur in most other alloys; these effects may obscure some of the behavior which we wish to understand better. A model for the solution of noble gases in liquid metals has already been proposed by us¹³ and shown to yield realistic results. In the following section, we will present an improvement on that model, one which yields a better estimate of the contribution of the dispersion forces to the molecular excess Gibbs energy of solution, ΔG^{XS} .

According to the model, ΔG^{XS} may be set equal to the total reversible isothermal work done in a sequence of three (conceptual) operations which transfer a solute molecule from its standard state in the gaseous phase into solution. These operations are as follows: (1) a solute molecule from the gas phase is confined to a small volume, δV , in which it exerts a pressure equal to the internal pressure of the solvent; the work done during this compression is denoted by w_{comp} ; (2) a spherical cavity of volume equal to δV is created in the solvent; the work done to form this cavity is denoted by w_{cav} ; (3) the molecule is inserted into the cavity, and in so doing, an amount of work (of negative sign) denoted by w_{attr} is done by the attractive forces acting between the solute molecule and the surrounding solvent. The excess molecular free energy of solution may be set equal to $w_{comp} + w_{cav} + w_{attr}$.

The previously described method¹³ of estimating w_{attr} has been improved. We still assume w_{attr} to be well approximated by the Linder formula¹⁴ for the generalized potential due to induced dipole-induced dipole forces, ϕ_{d-d} , felt by a single molecule (B) near or within a macroscopic body (A),

$$w_{attr} \approx \phi_{d-d} = -\frac{3}{4} \hbar \frac{\bar{\omega}_B \bar{\omega}_A}{\bar{\omega}_B + \bar{\omega}_A} \alpha_B(0) R_A(0) \quad (1)$$

where \hbar is Planck's constant divided by 2π , $\alpha_B(0)$ is the static electric dipole polarizability of the molecule in question, $R_A(0)$ is the static reaction field due to the macroscopic body, and $\bar{\omega}_B$ and $\bar{\omega}_A$ are the

¹³ H. M. Feder and H. C. Schnyders in Chemical Engineering Annual Report--1970, USAEC report ANL-7775, Section V.A.1.C (in press).

¹⁴ B. Linder in Advan. Chem. Phys., Vol. XII, p. 225, J. O. Hirschfelder, ed., Interscience Publishers, New York (1967).

frequencies at which the corresponding frequency-dependent functions $\alpha_B(\omega)$ and $R_A(\omega)$ have dominant resonances. The reaction field within a spherical cavity of radius a in a metallic conductor (assumed to be a continuum) is

$$R_A(0) = a^{-3} \quad (2)$$

and

$$\bar{\omega}_A = \frac{2}{3} \frac{1/2}{\omega_p} \quad (3)$$

where ω_p is the plasmon frequency of the metal. In our previous calculations, we used a method, due to Langhoff and Karplus,¹⁵ which fits optical dispersion data for gases in such a way as to provide upper and lower bound estimates for the resonant frequency, $\bar{\omega}_B$, of the solute molecule. These two estimates were substituted into Eq. 1 to give corresponding upper and lower bounds to w_{attr} , and we chose the arithmetic mean of these two values as our estimate of this quantity. However, this arbitrary choice was found to be unnecessary since $\bar{\omega}_B$ is conveniently related to the London induced dipole-induced dipole coefficient C_{d-d} . (The attractive interaction between a pair of molecules may be written as $-C_{d-d}/r^6$ for large values of the intermolecular separation, r .) This relation is

$$C_{d-d} = \frac{3}{4} \bar{\omega}_B [\alpha_B(0)]^2 \quad (4)$$

Both $\alpha_B(0)$ and C_{d-d} are accurately known from various experimental data on pure substances in the gas phase^{15,16}, and Eq. 4 can be rearranged to give a value for $\bar{\omega}_B$. We now believe this estimate of $\bar{\omega}_B$ to be a superior one and have used it in revised calculations of w_{attr} and Δg^{xs} .

The recalculated solubilities of the noble gases are compared with experimental values in Fig. I-5. Solubilities are presented in terms of the Ostwald coefficient, λ , the ratio of the concentration of solute in the liquid phase to the concentration of solute in the gaseous phase in equilibrium with it. The Ostwald coefficient, which may be calculated from the relation $\Delta g^{xs} = -k_B T \ln \lambda$, is related to the more frequently quoted solubility S (in units of ppb/atm) by the equation

$$S = 10^9 \frac{M_s \lambda}{dRT} \quad (5)$$

where d is the density of the solvent at the Kelvin temperature T , R the molar gas constant, k_B the Boltzmann's constant, and M_s the molecular weight of the solute.

¹⁵ P. W. Langhoff and M. Karplus, J. Chem. Phys. 53, 233 (1970).

¹⁶ J. A. Barker and P. J. Leonard, Phys. Letters 13, 127 (1964).

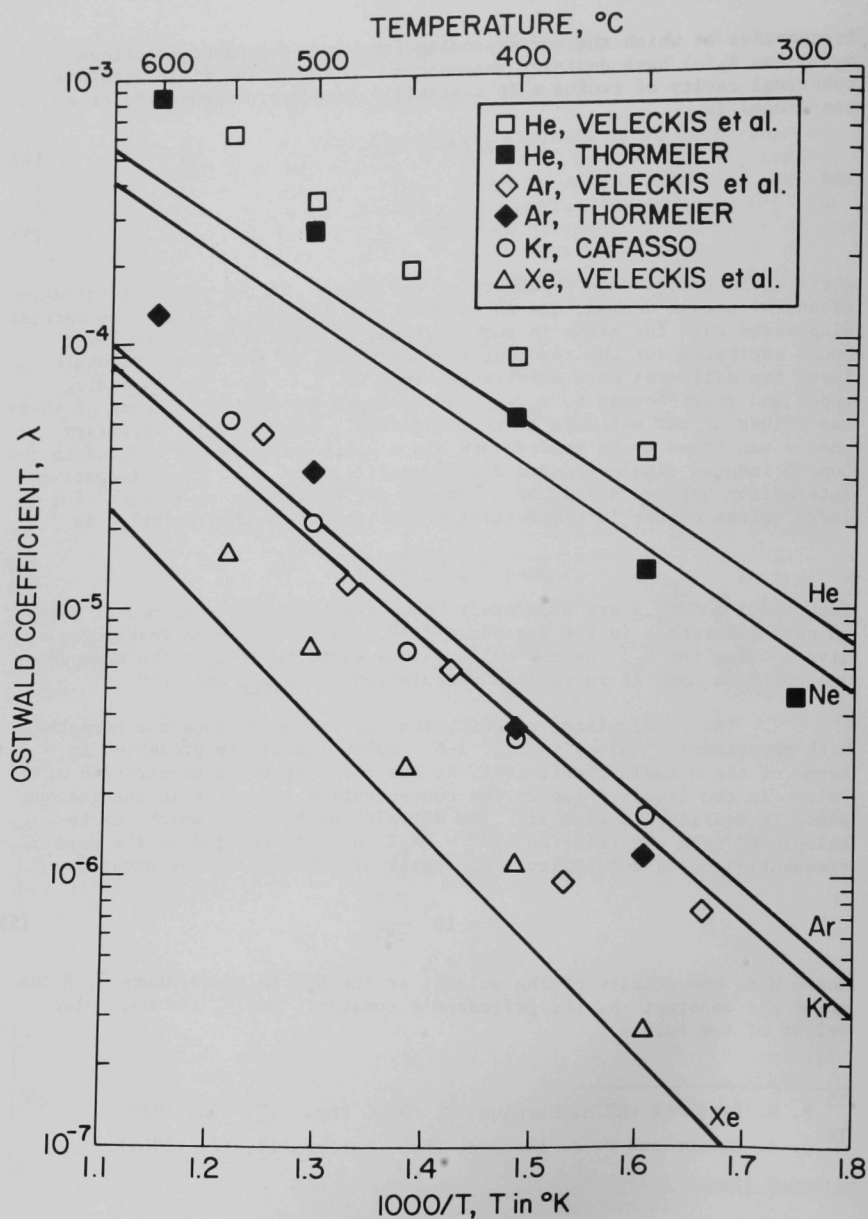


Fig. I-5. Ostwald Coefficients of Noble Gases in Liquid Sodium; Symbols Represent Experimental Results and Solid Lines Calculated Results

These calculations led us to believe that previously reported¹⁷ measurements of the solubility of krypton in liquid sodium were inaccurate. This suspicion turned out to be correct as more recent experimental solubilities¹⁸ are about a decade higher and show a temperature dependence more consistent with the measurements on other noble gases in liquid sodium. The recent data on krypton solubility in liquid sodium are displayed as open circles in Fig. I-5. The open squares, diamonds, and triangles in Fig. I-5 represent the experimental data of E. Veleckis et al. for helium,¹⁹ argon,²⁰ and xenon²¹ in liquid sodium, respectively. The data of K. Thormeier²² for helium and argon are designated by solid squares and diamonds, respectively.

The calculated solubilities of the noble gases in liquid sodium are displayed in Fig. I-5 as solid lines identified by the chemical symbol for the noble gas. The overall agreement with experimental results is reasonable but not perfect. Further refinements, such as consideration of the effect of higher-order multipolar contributions to w_{attr} , an orthogonality correction to allow for the non-penetration of ionic or solute cores by the conduction electrons, use of a soft-sphere equation of state to estimate w_{comp} , and use of a more accurate partition function to represent the motions of a dissolved solute atom, are all expected to give small, but not necessarily insignificant, contributions to Δg^{XS} . Inclusion of these effects in our model may remove the remaining discrepancies.

2. Equation of State of Polarizable Soft-Sphere Fluids

The work done, w_{attr} , by the attractive forces acting between the solute molecule and the solvent is a significant term in our model describing noble gas solubilities in liquid metals, but it is not the dominant term. Consequently, the comparison of our calculated results with the experimental data in these systems does not provide a means for ascertaining the accuracy of our calculation of this term. It occurred to us that many of the concepts employed in our model could equally well be applied to a model description of the cohesive free energies of the pure liquefied noble gases. The cohesive free energies for these materials are dominated by the potential energy due to London dispersion interactions. The appropriate application of the Linder formula (Eq. 1) to this problem should

¹⁷ S. K. Dhar, Solubility of Krypton in Liquid Sodium, in USAEC report ANL-6900, p. 125 (1964).

¹⁸ F. Cafasso and R. Blomquist, private communication.

¹⁹ E. Veleckis and G. Redding in Chemical Engineering Division Annual Report--1969, USAEC report ANL-7675, p. 64 (1970).

²⁰ E. Veleckis, R. Blomquist, R. Yonco, and M. Perin in Chemical Engineering Division Semiannual Report--July-Dec 1966, USAEC report ANL-7325, p. 128 (1967).

²¹ E. Veleckis and W. A. Kremsner in Chemical Engineering Division Annual Report--1970, USAEC report ANL-7775, Section II.A.3 (in press).

²² K. Thormeier, Atomkernenerg. 14, 449 (1969).

serve as a fairly sensitive test of its accuracy.²³

Consider one mole of a noble gas at temperature T and a molar volume v_g . The first step of our model process for the condensation of this gas will be the (conceptual) discharging of the attractive intermolecular forces at constant density (See Fig. I-6). The result is one mole of a gas of "soft" spheres (the molecules interact via long-ranged repulsive forces only) at v_g and T . The corresponding Helmholtz energy change for this process is

$$\Delta A_1 = -A_{\text{disp}}^g \quad (6)$$

The second step is the isothermal compression of the soft-sphere fluid from v_g to the molar volume of the real liquid v_ℓ , which is accompanied by a molar Helmholtz energy change of

$$\Delta A_2 = \Delta A_{\text{comp}} = A_\ell^{\text{xs}} - A_g^{\text{xs}} + RT \ln \frac{v_g}{v_\ell} \quad (7)$$

where A^{xs} is the molar excess Helmholtz energy of a soft-sphere fluid relative to the ideal gas at the same temperature and density. The last term in Eq. 7 is the well-known entropic change accompanying the compression of an ideal gas. In the third step, the attractive forces between molecules assumed to be exclusively induced dipole-induced dipole forces are "turned on" at constant density with a molar Helmholtz energy change,

$$\Delta A_3 = A_{\text{disp}}^\ell \quad (8)$$

The sum of Eqs. 6, 7, and 8 represents the molar Helmholtz energy at condensation. The fourth step is the isothermal vaporization of one mole of the liquid to the saturated vapor state (T, v_g). The Helmholtz energy change for this step is

$$\Delta A_4 = \Delta A_{\text{vap}} = \Delta G_{\text{vap}} - \Delta(PV) = -\Delta(PV) \quad (9)$$

since along the saturated vapor curve, the Gibbs energy change, ΔG_{vap} , equals zero by definition.

The sum of the Helmholtz energy changes for the four steps in the cyclic process must be zero, i.e.,

$$A_{\text{disp}}^\ell - A_{\text{disp}}^g + A_\ell^{\text{xs}} - A_g^{\text{xs}} + RT \ln \frac{v_g}{v_\ell} - P_s (v_g - v_\ell) = 0 \quad (10)$$

where we have replaced $-\Delta(PV)$ by $-P_s (v_g - v_\ell)$, P_s being the saturated vapor pressure. For convenience, we shall consider only saturated vapors at densities low enough for the ideal gas law to hold, i.e., $P_s v_g = RT$. (At greater densities of the vapor phase, one must use higher order terms

²³ A weak and inconclusive attempt was made by B. Linder, J. Chem. Phys. 33, 668 (1960); 34, 371 (1961).

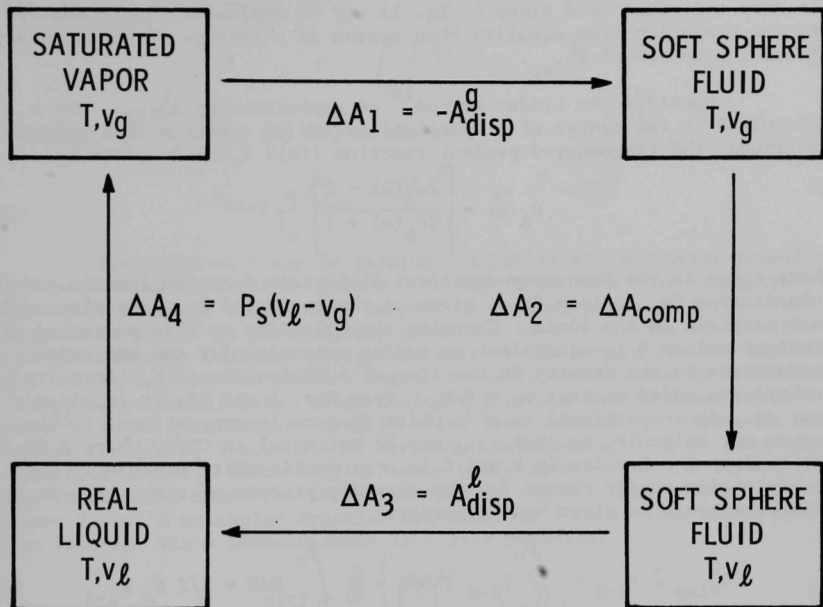


Fig. I-6. Helmholtz Energy Cycle for Model Process of Condensation

in the virial expression for $P_s v_g$.) For these low-density vapors, deviations from ideality being negligible, A_g^{xs} and A_{disp}^g may also be set equal to zero. One can then rearrange Eq. 10 as follows

$$-A_{disp}^{\ell} = A_{\ell}^{xs} + RT \left[\ln \frac{RT}{P_s v_{\ell}} + \frac{P_s v_{\ell}}{RT} - 1 \right] \quad (11)$$

The left and right hand sides of Eq. 11 may be evaluated independently, and the deviation from equality then serves as a measure of the accuracy of our evaluation of A_{disp}^{ℓ} .

Consider the Linder method¹⁴ of approximating A_{disp}^{ℓ} . For a molecule B in the center of a spherical cavity of radius a in a solvent continuum, the frequency-dependent reaction field $R_A(\omega)$ is given by

$$R_A(\omega) = \left[\frac{2\epsilon_A(\omega) - 2}{2\epsilon_A(\omega) + 1} \right] \frac{1}{a^3} \quad (12)$$

where $\epsilon_A(\omega)$ is the frequency-dependent dielectric function for the solvent. Substituting Eq. 12 into Eq. 1 gives us the potential ϕ_{d-d} experienced by each particle in the fluid. Charging the molecules to this potential at constant volume V is equivalent to adding molecules (at the potential appropriate to the density at the time of addition) until N_0 (Avogadro's number) are added so that $v_{\ell} = V/N_0$. From Eqs. 1 and 12, it is clear that ϕ_{d-d} is proportional to a^{-3} , which in turn is proportional to the volume per molecule, so that ϕ_{d-d} may be set equal to CN/V , where N is the number of molecules in V and C is a proportionality constant. Now the Helmholtz energy change for the charging process of step three in the Helmholtz cycle is given by the integral

$$A_{disp}^{\ell} \approx A_{d-d}^{\ell} = \int_0^{N_0} \phi_{d-d} (N) dN = \frac{C}{V} \int_0^{N_0} NdN = 1/2 N_0 \phi_{d-d} \quad (13)$$

The "solute" molecule B and the "solvent" molecule A being the same, $\bar{\omega}_A$ is equal to $\bar{\omega}_B$, and we may substitute Eq. 1 into Eq. 13 to obtain

$$A_{disp}^{\ell} \approx A_{d-d}^{\ell} = -3/16 \pi \bar{\omega}_A \alpha_A(0) R_A(0) \quad (14)$$

where $R_A(0)$ is evaluated at the density of the liquid. Once again $\bar{\omega}_A$ is conveniently calculated by Eq. 4.

Linder and Hoernschemeyer²⁴ have shown that there is a simple approximation which allows both the reaction field and the cavity field (which relates to the dielectric constant of the medium) within a spherical cavity in a medium to be calculated in a way which is consistent to the third order in polarizability. With the use of this approximation

²⁴ B. Linder and D. Hoernschemeyer, J. Chem. Phys. 46, 784 (1967).

$$R(0) = 2\theta \left(\kappa - \frac{\theta}{\sigma^3} \right) \quad (15)$$

where²⁵ $\theta \equiv 4\pi N_p \alpha(0)/3 v_l$, σ is the effective hard-sphere diameter of the molecule, and the quantity κ is related to the pair-distribution function, $g(R)$, of the liquid by

$$\kappa \equiv \int_0^\infty \frac{3 g(r)}{r^4} dr \quad (16)$$

Combining Eqs. 12, 15, and 16, we obtain

$$A_{\text{disp}}^l \sim A_{d-d}^l = \frac{-2\pi}{3} \frac{C_{d-d}}{v_l \sigma^3} (\kappa \sigma^3 - \theta) \quad (17)$$

The value of κ may be obtained either from the Fourier transform of experimental diffraction data on the liquid or from some consistent and reasonably accurate statistical mechanical approximation to $g(r)$. The integral in Eq. 16 is particularly sensitive to the details of how the pair-distribution function rises from zero at the origin towards its first peak at $r \approx 1.12\sigma$. The small r region of $g(r)$, as obtained by transformation of experimental data, often includes spurious oscillations about zero.²⁶ These oscillations usually arise from termination errors in the Fourier transform, i.e., lack of accurate experimental data at very high scattering angles. Therefore, it seems preferable to use the best available theoretical model for the evaluation of κ . For this purpose, we have chosen Verlet's molecular dynamics calculations²⁷ on a fluid whose particles interact via a Lennard-Jones 12-6 pair potential,

$$u(r) = 4\epsilon \left[\left(\frac{\sigma}{r} \right)^{12} - \left(\frac{\sigma}{r} \right)^6 \right] \quad (18)$$

where $-\epsilon$ is the value of $u(r)$ at its minimum (the bottom of the "well") and σ is the crossing point of $u(r)$, i.e., $u(\sigma) = 0$. Using Rahman's calculational technique, Verlet has determined the equilibrium pair distribution function $g(r)$ for such fluids at reduced temperatures, T^* ($= kt/\epsilon$) from 0.591 to 3.669, and reduced densities, ρ^* ($= \sigma^3/v_l$) from 0.450 to 0.880. We have taken the tabulated pair-distribution functions for 24 of these thermodynamic states of the fluid and performed the requisite integrations to obtain corresponding values for κ . These values of κ

²⁵ The subscripts distinguishing the solute and solvent will now be dropped.

²⁶ P. W. Schmidt and C. W. Tompson, Simple Dense Fluids, H. L. Frisch and Z. W. Salzburg, eds., Academic Press, New York (1968).

²⁷ L. Verlet, Phys. Rev. 165, 201 (1968).

were fitted to a function of T^* and ρ^* by stepwise regression.^{28,29} The resulting expression is

$$\begin{aligned} \frac{(\kappa\sigma^3)}{(\kappa\sigma^3)_{\rho=0}} &= 1 + a_0 \rho^* + a_1 \rho^* (T^*)^{-1/4} + a_2 T^* \rho^* \\ &+ a_3 (\rho^*)^2 + a_4 (\rho^*)^2 (T^*)^{1/4} \end{aligned} \quad (19)$$

where a_0 through a_4 are 2.517551, -2.87479, -0.056731, 1.057656, and -0.534079, respectively, and

$$(\kappa\sigma^3)_{\rho=0} = \frac{1}{4\sqrt{2}} (T^*)^{1/4} \sum_{m=0}^{\infty} \left[\Gamma\left(\frac{2m+1}{4}\right) \frac{2^m}{m!} (T^*)^{-\frac{m}{2}} \right] \quad (20)$$

(This expression is accurate to better than one percent within the range of Verlet's tables, but should not be extrapolated beyond that range.) In obtaining Eq. 18, we took advantage of the well-known property of $g(r)$, i.e., $g(r) \rightarrow \exp [-u(r)/kT]$ as $\rho^* \rightarrow 0$. In this limit, the defining equation for κ (Eq. 16) is exactly integrable³⁰ in terms of a series of gamma functions (Eq. 20). This constraint was applied in obtaining Eq. 19. For the evaluation of κ , use was made of the Lennard-Jones potential parameters, σ and ϵ , derived³¹ from second virial coefficient data.

After the attractive interactions are turned off in the vapor phase (step 1 in Fig. 1-6), we are left with a fluid of particles which interact via repulsive forces only. We shall assume a "soft-sphere" repulsive interaction of the form $4\epsilon (\sigma/r)^{24}$ with ϵ and σ both chosen as before. Such a choice is consistent, inasmuch as we believe the structure of a fluid, as given by $g(r)$, is basically determined by the repulsive part of the pair potential between molecules. Because the structure of liquid argon is well reproduced by the molecular dynamics results for a fluid interacting with a Lennard-Jones pair potential^{27,32} (Eq. 18) with

-
- ²⁸ N. R. Draper and H. Smith, Applied Regression Analysis, John Wiley & Sons, New York (1966).
- ²⁹ M. A. Efroymson, Mathematical Methods for Digital Computers, Vol. I, p. 191, A. Ralston, ed., John Wiley & Sons, New York (1960).
- ³⁰ A. D. Buckingham and J. H. Pople, Trans. Faraday Soc. 51, 1173 (1955).
- ³¹ H. Reiss, Advan. Chem. Phys. Vol. 9, p. 1, I. Prigogine, ed., Interscience Publishers, New York (1965); C. C. Lim, D. H. Bowman, R. A. Aziz, Can. J. Chem. 46, 3477 (1968); G. Boato, Casanova, Physica 27, 571 (1961).
- ³² L. Verlet, Phys. Rev. 159, 98 (1967).

the parameters fit to second virial coefficient data in the gas phase, we feel these parameters give an adequate description of the soft-sphere pair potential $4\epsilon (\sigma/r)^{24}$. The excess Helmholtz energy (relative to the ideal gas at the same temperature and density), A_k^{xs} , for a soft-sphere fluid interacting through a $4\epsilon (\sigma/r)^{24}$ pair potential has been recently calculated by Hoover et al.³³ via the Monte Carlo technique. We have fitted their tabular values for $(A^{xs}/N_0 kT)_\infty$ to a polynomial in $X = \rho^* \sqrt{2} (T^*)^{1/4}$,

$$(A^{xs}/N_0 kT)_\infty = b_1 X + b_2 X^2 + b_3 X^3 + b_4 X^4 \quad (21)$$

where b_1 through b_4 are 3.606420, 3.999548, 2.199512, and 3.963357, respectively. This expression is accurate to better than 0.3% at all points.

With the calculational methods described in the preceding paragraphs, we may now be able to compare the right-hand side (RHS) of Eq. 11 with $-A_{d-d}^k$ to test the accuracy of our estimate of the latter. Table I-3 gives the values of the molecular parameters used in these calculations. Table I-4 shows calculated values of $-A_{d-d}^k$ at two typical points along the orthobaric lines of argon, krypton, and xenon. (These are the noble-gas fluids for which quantum corrections are regarded as negligible.) Several points are evident from an examination of the tabulated results: First, to the extent that the RHS of Eq. 11 is accurate (the only important source of inaccuracy would be in the constants, ϵ and σ ,²⁴ and the form of the assumed repulsive potential), the induced dipole-induced dipole free energy given by the Linder formula (Eq. 17) is correct to better than 15%. An error of not more than 15% in the attractive term, w_{attr} , from Eq. 1 is tolerable in the calculation of the excess free energy of solution of a noble gas in a liquid metal at the present stage of refinement.

Secondly, if, again, the RHS of Eq. 11 is accurate, then Eq. 17 appears to consistently underestimate A_{disp}^k by from 5% for argon to 15% for xenon. This effect was not totally unexpected, inasmuch as the induced dipole-induced dipole interaction is not the whole of the dispersion energy, and contributions of the magnitude of the difference arise from the higher-order multipolar interactions, e.g., the induced dipole-induced quadrupole interaction. An effort is now being made to estimate these additional contributions to A_{disp}^k . In addition, an investigation must be made into the question of whether the centering hypothesis implicit in Eq. 12 is valid when the atom in question is thermally agitated away from its position of lowest potential energy (vibrational effect).

Thirdly, Eq. 11 can be rearranged to permit a calculation of P_s . This has been done and the results, with A_{d-d}^k substituted for A_{disp}^k , are

³³ W. G. Hoover, M. Ross, K. W. Johnson, D. Henderson, J. A. Barker, and B. C. Brown, J. Chem. Phys. 52, 4931 (1970).

Table I-3. Atomic Parameters of Noble Gases

Quantity	Reference	Argon	Krypton	Xenon
σ , Å	18	3.405	3.591	3.97
(ϵ/k) , °K	18	125.2	182.9	217
α_o , atomic units ^a	3	11.091	16.740	27.340
C_{d-d} , atomic units ^a	21	65.71	130.8	276.7

^a In atomic units, $\hbar = m = e = 1$.

Table I-4. Dispersional Helmholtz Energies of Argon, Krypton, and Xenon

Quantity	Argon		Krypton		Xenon	
T, °K	87.27	120	119.8	160	165.05	220
ρ_ℓ , g/cm ³ (Ref. 34)	1.3998	1.160	2.413	2.072	3.057	2.642
(A_ℓ^{xs}), cal/mol	913	762	1202	1072	1829	1449
RHS (Eq. 11), cal/mol	1697	1290	2309	1871	3389	2594
($-A_{\text{d-d}}^\ell$), cal/mol	1617	1224	2175	1719	2884	2238
P_s (exp.), atm (Ref. 34)	1.00	11.98	1.00	10.0	1.00	10.0
P_s (calc.), atm	1.6	16.0	1.8	16.4	4.7	23.5

³⁴ J. A. Barker and P. J. Leonard, Phys. Letters 13, 127 (1964).

compared with experimental values³⁵ of P_s in the last two rows of Table I-4. Calculation of the orthobaric pressure is a very sensitive test of the accuracy of any theoretical model employed to calculate the cohesive free energy of noble-gas liquids. In order to predict vapor pressures to within 10%, free energy estimates must be accurate to within 30 cal/mol. It is not unlikely that accuracy of this order may be attained when the refinements indicated in the preceding paragraph are properly made.

³⁵ A. C. Hollis Hallett, Argon, Helium, and The Rare Gases, Vol. 1, p. 324, G. A. Cook, ed., Interscience Publishers, New York (1961).

II. MOLTEN SALT STUDIES (E. J. Cairns)

Broad understanding of the physicochemical properties of molten salts continues to be of importance because of their extensive use in many AEC and industrial applications. The Chemical Engineering Division has been conducting research relating to the thermodynamics of binary and multicomponent salt and salt-metal systems. Investigations into the structure of species present in molten-salt media are also being carried out.

A. Thermodynamics

Experimental and theoretical studies dealing with molten-salt systems have formed an on-going program in the Chemical Engineering Division. Whereas most previous work has dealt with all salt or salt-metal systems, recent work has concentrated on the behavior of systems involving the interaction of salts and semimetals or nonmetals. This work has particular application in electrochemical energy conversion and storage devices using alkali metal-chalcogen couples.

1. Thermodynamics of Pseudo-Ternary Lithium Chalcogenide-Chalcogen-Alkali Halide Systems by EMF Methods

a. Selenium-Containing Systems (E. J. Cairns, G. H. Kucera, P. D. Hunt)

Ambiguities arising in attempts to correlate emf data from reversible electrochemical cell work with phase diagram studies in lithium selenide-selenium systems have shown that it is necessary to include the influence of the electrolyte on emf cell behavior. The reason for this influence is the significant mutual solubility of the halide electrolyte and the lithium-rich liquid (L_2) in the lithium-selenium system.³⁶ Consideration of the electrolyte mixture as one component in a pseudo-ternary lithium selenide-selenium-electrolyte (halide eutectic) system leads to a phase diagram which is consistent with all of the experimental observations on this system.

EMF measurements on the $\text{Li/LiBr-RbBr (eutectic)/Li in Se}$ cell at 360°C have been conducted in the high selenium-low salt composition region using a modification of the Type II, three-compartment H cell which has been described previously.³⁷ Modifications were incorporated in the cell in order to accommodate the selenium-rich compositions. As shown in Fig. II-1, a cylindrical quartz displacement body was placed in the cathode chamber to provide for increased selenium-to-salt ratios ($n_{\text{Se}}/n_{\text{Se}} + n_{\text{P}}$) and also to allow for accommodation of the lithium electrochemically transferred from the anode to the cathode compartment of the cell. A niobium

³⁶ Chemical Engineering Division Annual Report--1970, USAEC report ANL-7775, Sec. V.A.1.a(1) (in press).

³⁷ Ibid., Section V.B.1.c.

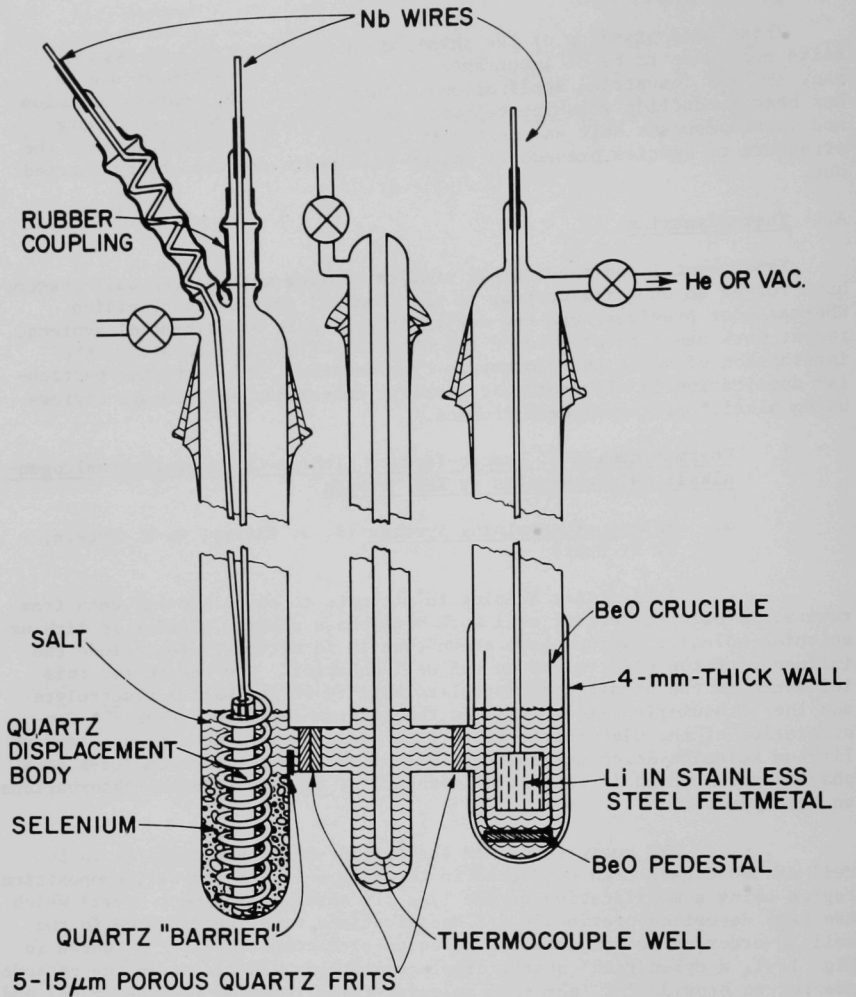


Fig. II-1. Schematic Diagram of Cell Used in Studying Effect of Alloy Composition on Emf for Selenium-Containing Systems

wire was attached to the displacement body (which is fully inserted into the cathode chamber at the initial stage of each experiment) and passed through a port provided in the Pyrex cap of the cathode chamber. The displacement body was raised by making bends in the niobium wire through the rubber coupling. The level of the electrolyte in the cathode compartment was controlled by adjustment of the position of the displacement body. Additional design changes from the cell described previously were an increase in the cathode compartment capacity in order to contain more selenium, employment of a double thickness of extra-fine (5-15 μm) porous quartz frit between the center and cathode chambers (to retard diffusion of selenium), use of a thicker quartz wall (approximately 4 mm thick) in the lower 15-cm portion of the anode compartment to accommodate some lithium metal attack, and the addition of a small quartz barrier between the cathode and center chambers to reduce the amount of salt necessary in the cathode chamber.

The equipment used to measure and monitor the cell emf and to supply the constant current necessary for changing the composition of the lithium-selenium alloy has been described elsewhere.³⁶ The currents used for discharging the cell were generally between 10 and 60 mA; however, several compositional changes were effected successfully at 90 to 100 mA.

The emf experiments in the selenium-rich region of this system did not include a detailed study of the temperature coefficient of emf. The sign of the temperature coefficient of emf was in accord with previous observations at a $n_{\text{Se}}/(n_{\text{Se}} + n_{\text{E}})$ ratio of 0.384. That is, for a lithium content $x_{\text{Li}} \equiv n_{\text{Li}}/(n_{\text{Li}} + n_{\text{Se}})$, below 0.13, (dE/dT) is positive; in the range 0.15 to 0.28, $(dE/dT) = 0$; and for 0.32 and greater, (dE/dT) is negative.

The emf values of three Li/LiBr-RbBr (eutectic)/Li in Se cells as a function of cathode composition are presented in Fig. II-2 for a temperature of 360°C. In the right-hand portion of Fig. II-2, the data are presented on a linear scale of emf vs. atom percent of lithium in selenium in the cathode compartment. The principal utility of this type of plot is in locating the intersections of the straight-line regions at the higher lithium concentrations. Comparison of the emf data show good consistency among the data for cells of different $n_{\text{Se}}/(n_{\text{Se}} + n_{\text{E}})$ ratios. Notably, in the dilute-lithium region designated $L_1 + L_3$ (L_1 , L_2 , and L_3 refer to liquid fields in the pseudo-ternary phase diagram; see Fig. II-4), the slopes of emf vs. logarithm of composition exhibit the Nernst slope, RT/nF corresponding to ~ 63 mV/decade. This slope is required for a two-electron ($n = 2$) reaction, which may be written: $2\text{Li} + x\text{Se} \rightarrow \text{Li}_2\text{Se}_x$. In the three-phase region labeled $L_1 + L_2 + L_3$, the slight downward trend of emf vs cathode composition (which should be horizontal for a three-phase region in a three-component system) is thought to be caused by exchange of rubidium and lithium at the electrolyte-cathode interface in the cathode chamber. The formation of some Rb_2Se_x would be expected to lower the cell potential slightly as the lithium concentration increases in the cathode alloy. The discontinuous changes in the slopes $dE/d\ln x_{\text{Li}}$ denote the locations of phase boundaries. For Cell No. 2164F-72, a change in slope occurs at $x_{\text{Li}} = 0.04$; Cells No. 2258F-32 and 2258F-41 show phase boundaries indicated by changes of slope at $x_{\text{Li}} = 0.023$, $x_{\text{Li}} = 0.252$ and $x_{\text{Li}} = 0.298$.

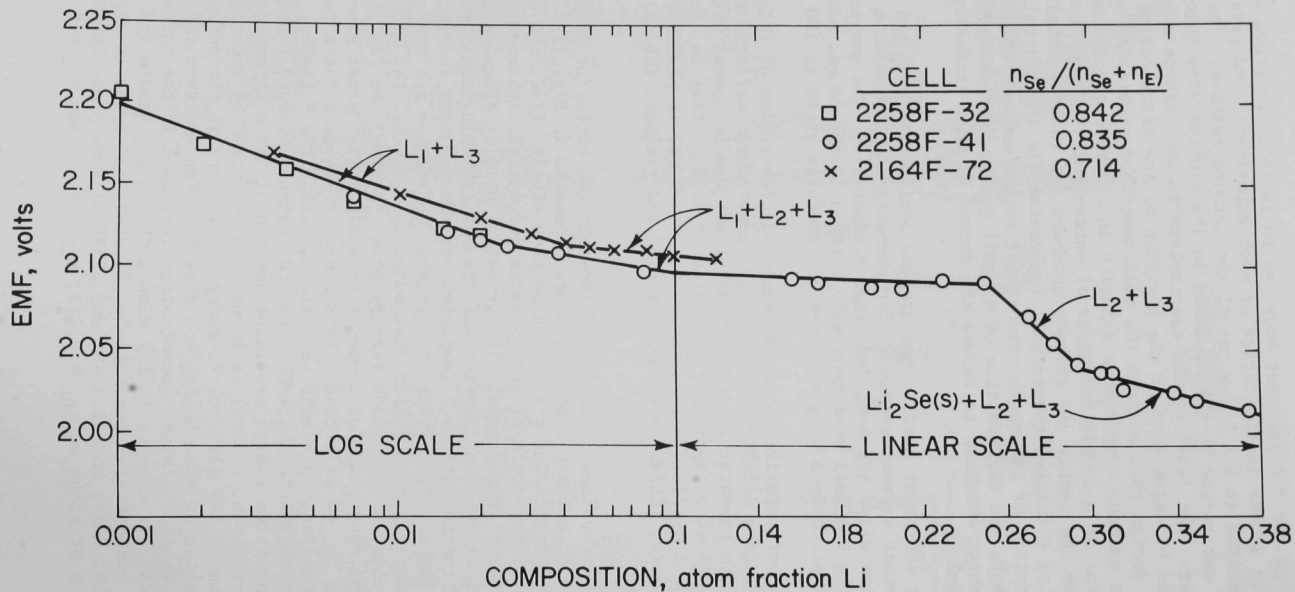


Fig. II-2. Emf Measurements at 360°C as Function of Cathode Composition for Three Li/LiBr-RbBr/Li in Se Cells

Failure of the cell due to lithium attack on the anode compartment terminated collection of emf measurements in Cell No. 2164F-72 at $x_{Li} = 0.12$. Cell No. 2258F-32 failed for similar reasons after reaching $x_{Li} = 0.02$. The integrity of Cell No. 2258F-41 was maintained through the $L_2 + L_3$ phase field and into the region $Li_2Se(s) + L_2 + L_3$ ($x_{Li} = 0.375$). As in the $L_1 + L_2 + L_3$ region, this three-phase area emf should be invariant with respect to composition in accord with the phase rule. The rubidium in the electrolyte could exchange with lithium in L_2 , causing a slight downward trend with increasing x_{Li} , particularly at high $n_{Se}/(n_{Se} + n_E)$ ratios. Experiments conducted with only lithium cations in the electrolyte have not shown this downward trend.³⁷ Another effect at high selenium-to-salt ratios was the formation of appreciable amounts of solid Li_2Se during discharge, which require considerable periods of time for dissolution and, therefore, for emf equilibration. At $x_{Li} = 0.34$ and 0.375 , the cell potential rose at rates of less than 0.1 mV/hr as equilibrium was approached. The time required to obtain each measurement was 5 to 6 days.

The highest $n_{Se}/(n_{Se} + n_E)$ ratio studied was 0.903 (Fig. II-3). Distinct changes in slope occurred at $x_{Li} = 0.008$ and 0.152 . The slope for the low x_{Li} region is in agreement with both the previous data obtained in the $L_1 + L_3$ region and the Nernst slope of $RT/2F$. After passing through the $L_1 + L_2 + L_3$ phase region and into the $L_1 + L_2$ region, the cell potential continued to increase at a low rate (~ 0.5 mV/hr) to unreasonably high values. This behavior was probably caused by the absence of L_3 in the cathode compartment, resulting in a relatively large driving force for the transfer of L_3 (or electrolyte) from the center compartment into the cathode chamber, and conversely of L_2 into the electrolyte contained in the center compartment. Under such circumstances, the cell potential would be influenced by the composition in the quartz frit separator rather than by the composition of the bulk of the cathode alloy. To circumvent this problem, one could utilize a solid lithium-ion-conducting electrolyte, e.g., $Li_2O \cdot 11 Al_2O_3$, which would prevent diffusion of any material from the cathode compartment.

The various phase regions and boundaries determined by changes in slope for the above-discussed emf versus composition plots can be understood on the basis of the pseudo-ternary phase diagram shown in Fig. II-4. The results shown in Fig. II-2 for $n_{Se}/(n_{Se} + n_E) = 0.714$ (Cell No. 2164F-72) correspond to a line parallel to the Li_2Se -Se side of the diagram at 71.4 mol% Se in Fig. II-4. The values for x_{Li} corresponding to changes in slope (indicating phase boundaries) have been converted to mole percent Li_2Se . All available data are summarized in Table II-1. Using these data, the phase boundaries shown in Fig. II-4 were located and are found to conform with the results of thermal analyses³⁷ and centrifugation experiments (See Section II.A.2 of this report).

It can be seen from Fig. II-4 that, at $360^\circ C$, L_1 is selenium containing small concentrations of salt (< 0.02 mol%)³⁸ and lithium

³⁸ Chemical Engineering Division Annual Report--1970, USAEC report ANL-7775, Section V.B.1.a. (in press).

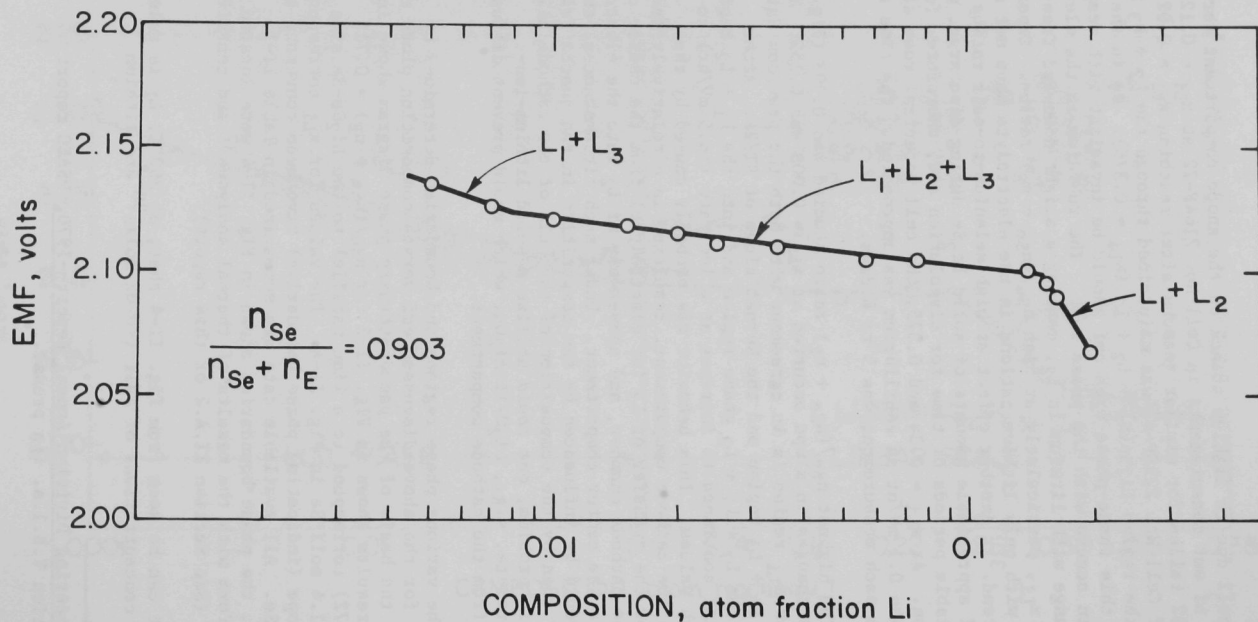


Fig. II-3. Emf Measurements at 360°C as Function of Cathode Composition for Li/LiBr-RbBr/Li in Se Cell with $n_{Se}/(n_{Se} + n_E) = 0.903$

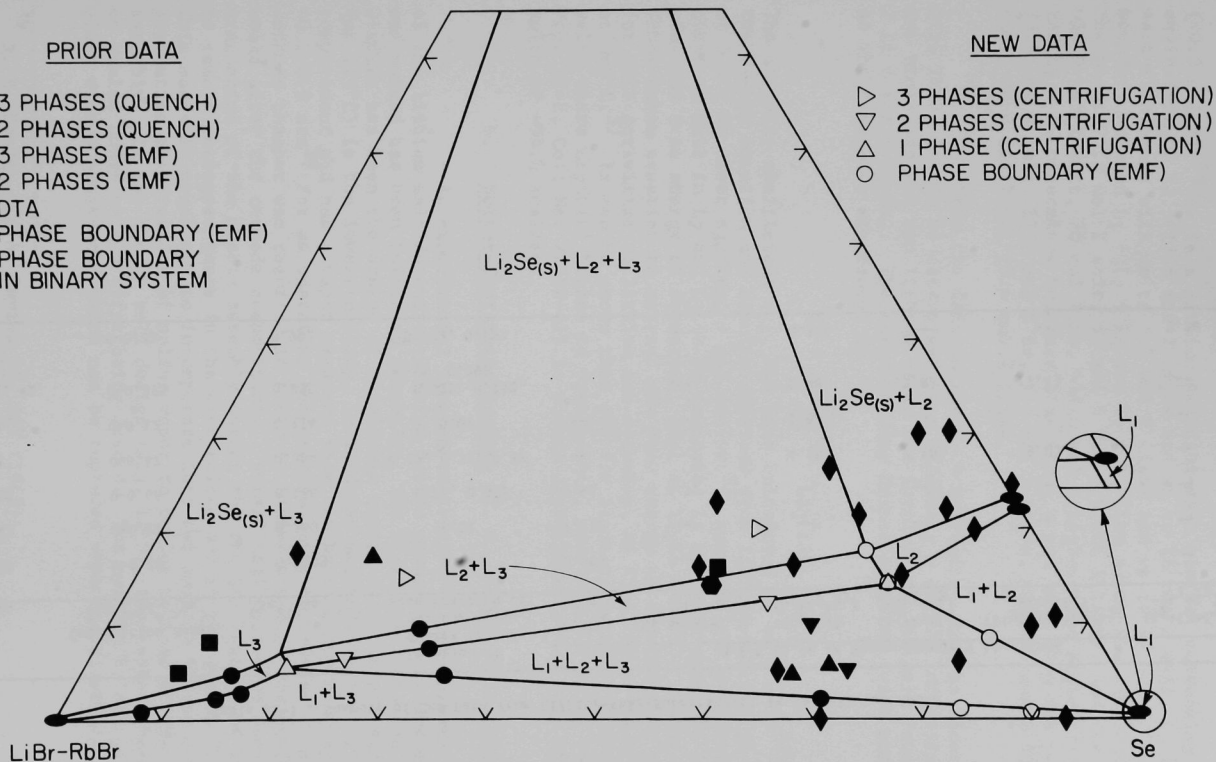


Fig. II-4. Li₂Se-Se-(LiBr-RbBr Eutectic) Pseudo-Ternary Phase Diagram [Details of Differential Thermal Analysis (DTA) Data Are Contained in ANL-7775, Fig. V-17]

Table II-1. Summary of Emf Data from Li/LiBr-RbBr(Eutectic)/Li in Se Cells at 360°C

Cell No.	Composition Range, $n_{Li}/(n_{Li} + n_{Se})$	$n_{Se}/(n_{Se} + n_E)$	Location of Breaks in Emf vs. Log x_{Li} , Atom Fraction Li	Mol % Li_2Se at Phase Boundary Locations					
				(Li_1+Li_3) $-Li_3$	$(Li_2Se(s)+Li_3)$ $-Li_3$	(Li_1+Li_3) $-(Li_1+Li_2+Li_3)$	$(Li_1+Li_2+Li_3)$ $-(Li_2+Li_3)$	$(Li_2Se(s)+Li_2+Li_3)$ $-(Li_2+Li_3)$	$(Li_1+Li_2+Li_3)$ $-(Li_1+Li_2)$
2097F-129	0-0.28	0.0838	0.105	0.493	--	--	--	--	--
2097F-147	0-0.21	0.160	~0.21	~2.13	--	--	--	--	--
2097F-189	0-0.46	0.188	0.24, 0.335	2.96	4.72	--	--	--	--
2164F-18	0-0.47	0.384	0.19, 0.27, 0.32	--	--	4.50	7.10	9.03	--
2164F-72	0-0.12	0.714	0.04	--	--	1.64	--	--	--
2258F-32, 41	0-0.375	0.835	0.023, 0.252, 0.298	--	--	0.98	13.82	17.43	--
2258F-5	0-0.21	0.903	0.008, 0.152	--	--	0.326	--	--	8.28

(<0.5 mol %);³⁸ L_2 is a lithium-selenium-salt mixture containing the equivalent of 13.5-17.5 mol % Li_2Se and up to 16 mol % salt; L_3 is the salt-rich phase with up to 5.5 mol % Li_2Se and up to 19 mol % Se. The boundary between $L_1 + L_2 + L_3$ and $L_2 + L_3$ lies along the tie line from the point 75.5 mol % salt, 19 mol % Se, 5.5 mol % Li_2Se , and the point ~16.0 mol % salt, 70 mol % Se, ~14.0 mol % Li_2Se . The $Li_2Se(s) + L_2 + L_3$ and $L_2 + L_3$ coterminal boundary lies along a tie line from the point 75.5 mol % salt, 17.5 mol % Se, 7.0 mol % Li_2Se , and the point 16.0 mol % salt, 66.4 mol % Se, 17.6 mol % Li_2Se .

From the data in the $L_1 + L_2$ region, such as those of Fig. II-2, it can be determined that $dE/d\ln x_{Li} = RT/2F$, indicating that two electrons and two lithium atoms are involved in the cell reaction, $2 Li + xSe + Li_2Se_x$. The corresponding Nernst equation (with pure lithium as the reference electrode) is

$$E = - \frac{RT}{2F} \ln \gamma_{Li_2} x_{Li_2}$$

The activity coefficient γ_{Li_2} has been calculated to be 6×10^{-32} from the Nernst equation and results obtained from $Li/LiBr-RbBr/Li$ in Se cells at 360°C at lower $n_{Se}/(n_{Se} + n_E)$ ratios.³⁷ Assuming the activity coefficient of salt in L_2 and L_3 to be constant, it has been possible to determine the free energy of formation, ΔG_f , of Li_2Se (360°C). Using the Gibbs-Duhem equation to correct the free energy of formation to the value for unit activities of lithium and selenium, we find $\Delta G_f^\circ = -94.0$ kcal/mol at 360°C.³⁷ It can be shown that ΔG_f° for $Li_2Se(s)$ determined from the emf value where $Li_2Se(s)$ begins to precipitate, namely 2.042 volts (see Fig. II-2, Cell No. 2258F-41) is within approximately 0.3 kcal of the value of -94.0 kcal/mol.

b. Sulfur-Containing Systems (E. J. Cairns, G. H. Kucera)

An experimental program to study the thermodynamic behavior of the lithium sulfide-sulfur-lithium halide pseudo-ternary system by an emf method has been initiated recently. The first consideration in these studies has been the design of a suitable quartz cell. Since sulfur (mp 119°C) is the lowest-melting, least-dense material in the cathode compartment and has a vapor pressure that can be expected to vary from ~0.2-0.9 atm³⁹ for an operating temperature range of 360-440°C, a special cathode chamber was required in order to minimize sulfur losses (which would alter the cathode composition). Normal cell operation includes an evacuation of the quartz assembly during the initial heating of the cell to remove entrapped gases in the electrolyte and in the quartz frits. This makes it necessary to incorporate into the cathode holder a way of preventing the transfer of sulfur vapor to cooler regions of the cell assembly. In the chosen cell design (Fig. II-5), the cathode holder can be sealed under vacuum after being loaded. The cathode holder is provided with a break-seal which can be ruptured when the electrolyte

³⁹ R. E. Honig, R.C.A. Review 23, 567 (1962).

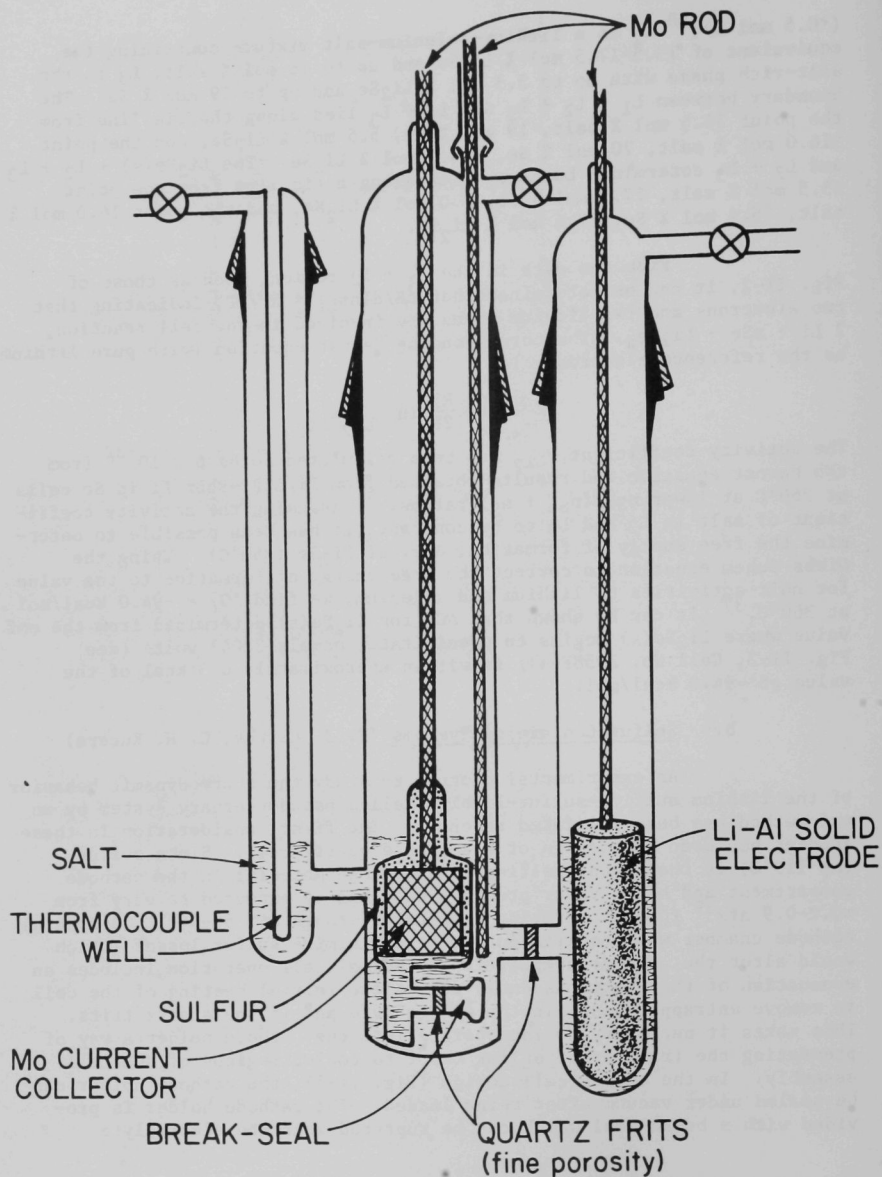


Fig. II-5. Schematic Diagram of Cell Used in Studying Effect of Alloy Composition on Emf for Sulfur-Containing Systems

(mp 341°C) surrounding the holder is molten. The cell assembly, which contains high-purity helium at a pressure of about one atmosphere, consists of three separate compartments with a quartz frit between the anode and cathode chambers to act as a diffusion barrier.

Generally, the emf cells have utilized a lithium-soaked Feltmetal sponge as a reference electrode;³⁷ however, evidence of lithium attack on the anode chamber walls has been found in these cells when the operating temperature has approached ~400°C. The reduction of the lithium activity in the electrolyte in this series of emf cells therefore becomes an important consideration. The use of a solid lithium-aluminum alloy as the counter electrode and reference electrode can be considered as a reasonable approach to this difficulty.

A lithium-aluminum alloy electrode was prepared by the electrochemical transfer of lithium into a solid cylinder of aluminum until a composition of ~42 at.% lithium in aluminum was obtained. The alloy electrode thus prepared, which had a surface area of ~24 cm², was capable of delivering current densities of ~170 mA/cm². Normal emf cell operation will require current densities of ~2 mA/cm² from this electrode to achieve the cathode alloy compositional changes.

Since the experimental cell will be operated over a range of temperatures, a study of the temperature dependence of the emf of the lithium-aluminum electrode versus a pure lithium electrode was made. A plot of the emf data collected over the temperature range 357-521°C, shown in Fig. II-6, resulted in a straight line and will be used to convert the emf obtained from Li(Al)/S cells to the emf of the corresponding Li/S⁴⁰ cell. An extrapolation of the emf data collected by N. P. Yao et al., who studied the same system over a temperature range of ~280-390°C, is found to coincide with the data obtained in our study.

Since solubility studies indicate a marked increase in the solubility of the sulfur in the LiBr-RbBr eutectic electrolyte in the presence of lithium sulfide,³⁸ it will be necessary to include the influence of the electrolyte on the behavior of these emf cells. A similar situation was seen in the lithium/selenium system, where it was necessary to consider the cathode not as a simple binary system but rather in terms of a pseudo-ternary system consisting of lithium selenide, selenium, and the alkali halide eutectic electrolyte.

2. Phase Diagram of the Pseudo-Ternary Lithium Selenide-Selenium-Alkali Halide System (V. A. Maroni, E. J. Hathaway)

Phase-equilibrium studies have been conducted to determine the compositions of the terminal phases in the Li₂Se-Se-(LiBr-RbBr eutectic) pseudo-ternary system. Some difficulties in separating the various

⁴⁰ N. P. Yao, L. A. Herédy and R. C. Saunders, J. Electrochem. Soc. 118, 1039 (1971).

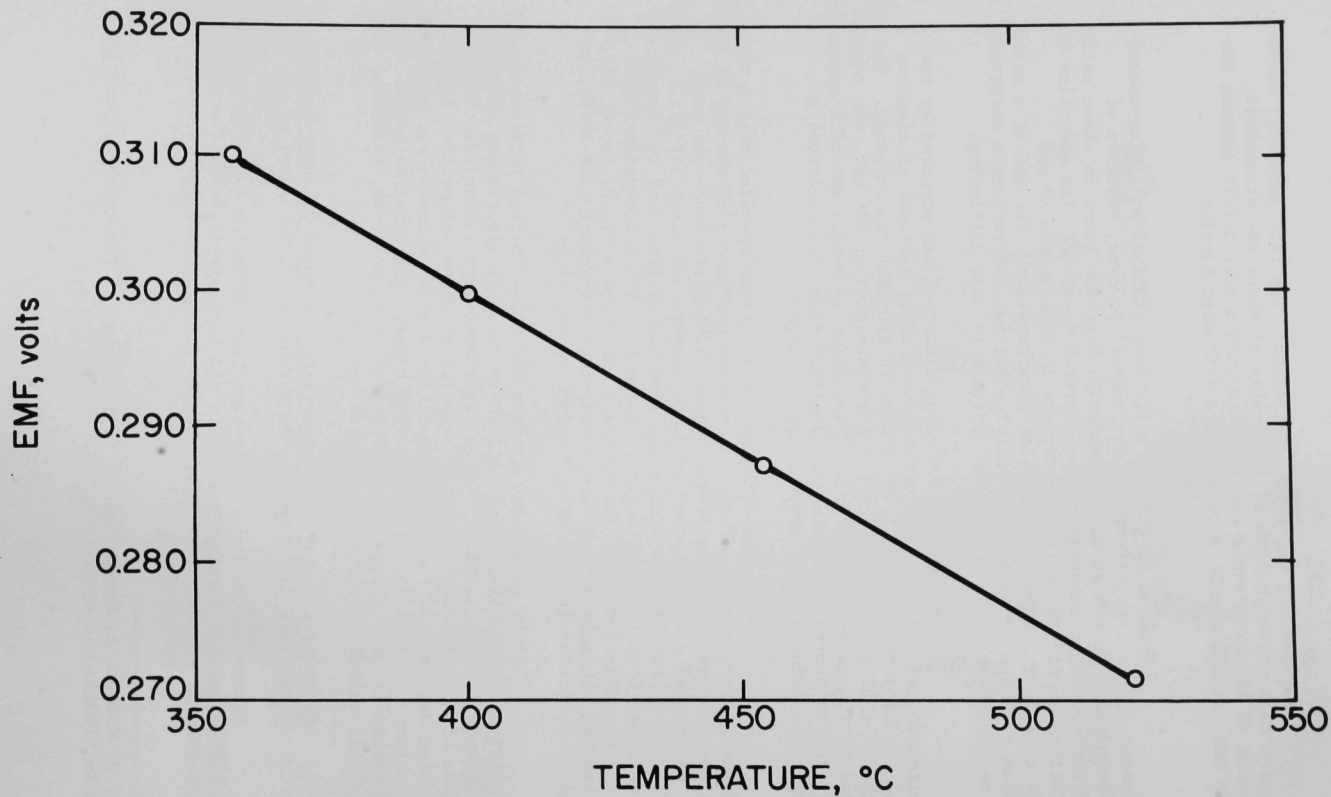


Fig. II-6. Emf as Function of Temperature for Li/(42 at. % Li-Al) Alloy Couple

liquid and solid phases were encountered in early experiments. In particular, the Li_2Se -rich and salt-rich liquid phases appeared to form emulsions in one another and would not separate even after standing times of up to several days. To effect the separation of the phases in equilibrium samples, a high-temperature centrifuge assembly, similar in design to one described by Friedmann,⁴¹ was constructed. A drawing of this assembly is shown in Fig. II-7. Samples of the desired composition were loaded into quartz tubes, sealed under vacuum, and equilibrated at temperatures of about 400°C in a rocker furnace for times in excess of 24 hr. The equilibrated samples were then removed from the quartz tubes, ground to a fine powder, and loaded into special quartz ampuls, which were placed in metal holding buckets. The buckets were then attached to the centrifuge. The samples were heated to 360°C and centrifuged for 8 to 10 hr periods at speeds in excess of 1200 rpm and with a minimum centrifugal force on the sample of 100 g . The temperature in the sample compartment of the centrifuge was found to vary by less than 2°C during operation. After centrifugation, the holding buckets (containing the ampuls) were removed from the mounting collar and immersed in liquid nitrogen. In most cases all of the samples could be removed from the centrifuge and quenched in less than 2 min from the time at which the furnace was opened. Centrifuged samples consistently showed nearly quantitative separation of all of the constituent phases. The selenium-rich liquid (liquid 1) was always found to be the most dense phase with the Li_2Se -rich liquid phase (liquid 2) intermediate and the salt-rich phase (liquid 3) the lowest-density phase. In cases where solid Li_2Se was present, it appeared in the upper portion of the salt-rich liquid phase.

To determine the appropriate compositions of the phases in equilibrium in a particular region of the phase diagram, samples from that region were centrifuged and portions of each of the separated phases were submitted for chemical analysis. With this technique, the compositions of the terminal phases were only roughly located ($\pm 5\%$) due to uncertainties in the analytical techniques. To pinpoint the locations of the phase boundaries more accurately, mixtures of Li_2Se , Se, and LiBr-RbBr eutectic with compositions in the vicinity of the analytically determined values for the terminal phases were equilibrated, centrifuged, and examined microscopically until a nearly single-phased sample was produced.

Thus far, as a result of these studies, the compositions of the corners of the three-liquid region have been located and the number and types of phases present at various locations throughout the diagram have been determined. These results are plotted in Fig. II-4 together with results from DTA, emf, and quenching studies; the data from the centrifugation experiments appear to be in good agreement with the results of other studies.

B. Structure Investigations by Spectroscopic Methods (V. A. Maroni, E. J. Hathaway)

The program of Raman spectroscopic studies has added much to our knowledge of the structure of molten salts. The existence of complex equilibria in Mg(II) - and Pb(II) -halide systems has been demonstrated,

⁴¹ H. A. Friedman, J. Sci. Instrum. 44, 454 (1967).

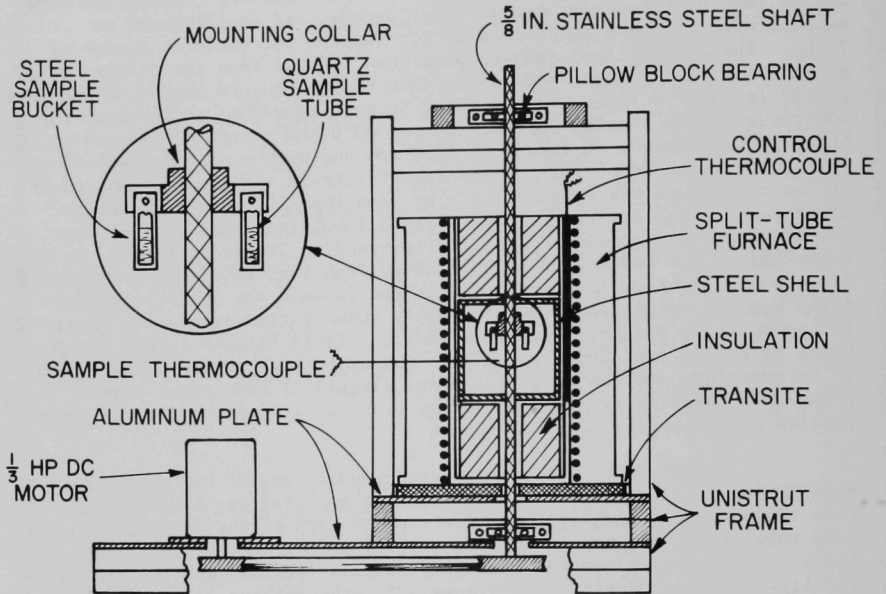


Fig. II-7. Schematic Diagram of High-Temperature Centrifuge Assembly

and in some cases the structures of the predominant complexes have been elucidated. Studies of polyatomic anions and their interaction with various cations in the molten state have revealed pertinent information on the nature of contact "ion-pairs" and cation polarization effects. These studies contribute to a better understanding of transport properties, distribution coefficients, and phase-equilibrium behavior in molten-salt systems. Recent results have been of particular importance to nuclear fuels reprocessing programs, studies of species in contact with liquid sodium, and systems of potential utility as galvanic cell cathodes.

The program of structural studies by Raman spectroscopy has been greatly facilitated over the past year by the acquisition of a powerful multifrequency laser, the Coherent Radiation Laboratories MG-52 mixed gas (argon-krypton) ion laser. With the new laser, the sensitivity of the spectrophotometer has been increased by over an order of magnitude, and our ability to examine colored solutions has been expanded.

1. Studies of Divalent Metal Halide Melts

Raman investigations of divalent metal halide melts have continued with the completion of studies on the $\text{MgBr}_2\text{-KBr}$, $\text{MgI}_2\text{-KI}$, $\text{PbCl}_2\text{-KCl}$, and $\text{PbBr}_2\text{-KBr}$ systems. The results of Raman spectroscopic and normal-coordinate examinations for the $\text{MgCl}_2\text{-KCl}$ system (reported previously in ANL-7775, Section V.B.2) confirmed the existence of tetrahedral MgCl_4^{2-} . These studies have since been extended to include $\text{MgBr}_2\text{-KBr}$ and $\text{MgI}_2\text{-KI}$ melts. Complete Raman spectra of MgBr_4^{2-} and MgI_4^{2-} , obtained for melts with a halide/magnesium (II) mole ratio of 4.0, are shown in Figs. II-8 and II-9, respectively, and the observed frequencies are listed in Table II-2. As in the case of MgCl_4^{2-} , one high-intensity polarized band and three low-intensity depolarized bands are observed for the bromide and iodide complexes. Normal-coordinate analyses were carried out for each of these species based on a tetrahedral configuration and using a Urey-Bradley force field⁴² with the conditions $F' = -0.1F$ and $H = 0$. Matrix elements used in the calculations were identical to those given by Nakamoto.⁴³ The calculated frequencies for MgBr_4^{2-} and MgI_4^{2-} are given in Table II-2 together with those previously determined for MgCl_4^{2-} , and the force constants for all three species are listed in Table II-3. Using the known relationships⁴³

$$f_r + 3f_{rr} = K + 4F \quad (1)$$

$$f_r - f_{rr} = K + 1.2F \quad (2)$$

and the results in Table II-2, the value of the generalized valence force

⁴² K. Nakamoto, Infrared Spectra of Inorganic and Coordination Compounds, p. 55, John Wiley & Sons, New York (1970).

⁴³ Ibid., p. 318.

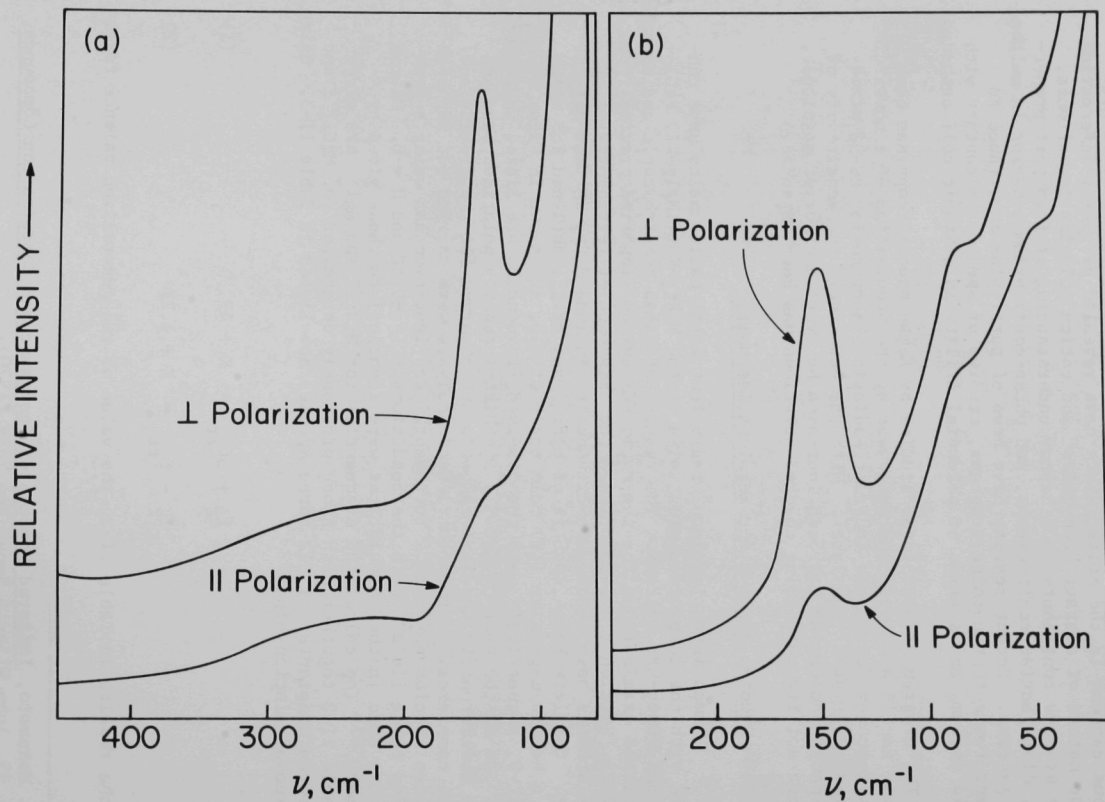


Fig. II-8. Raman Spectrum of Molten $\text{MgBr}_2\text{-KBr}$ ($\text{Br}^{1-}/\text{Mg}^{2+}$ Mole Ratio = 4.0) at 400°C ;
 Exciting Radiation = 4880 \AA for Curve (a) and 5682 \AA for Curve (b);
 || = Parallel Polarization, \perp = Perpendicular Polarization

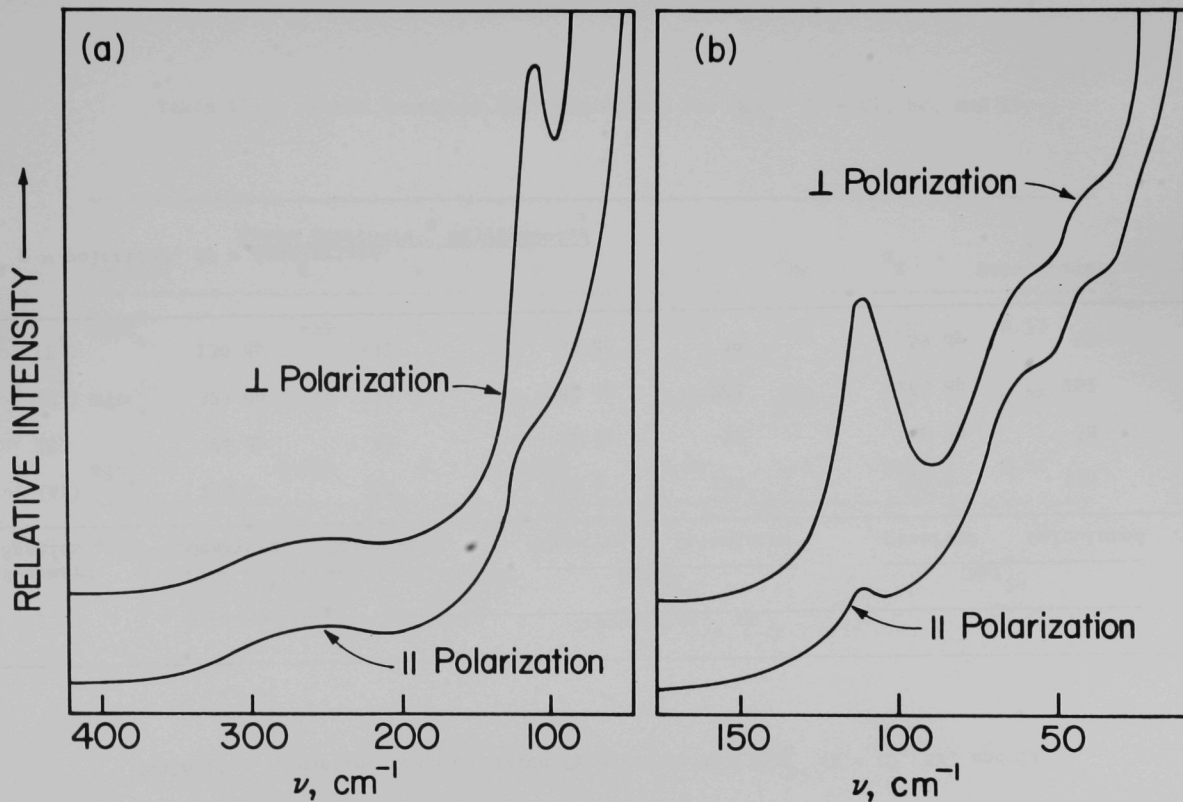


Fig. II-9. Raman Spectrum of Molten $\text{MgI}_2\text{-KI}$ ($\text{I}^{1-}/\text{Mg}^{2+}$ Mole Ratio = 3.5) at 400°C ;
 Exciting Radiation = 5145 \AA for Curve (a) and 6471 \AA for Curve (b);
 || = Parallel Polarization, \perp = Perpendicular Polarization

Table II-2. Observed and Calculated Frequencies for MgX_4^{2-} (X = Cl, Br, and I)

Symmetry Species	Frequencies, ^a cm ⁻¹					
	MgCl_4^{2-}		MgBr_4^{2-}		MgI_4^{2-}	
	Observed	Calculated	Observed	Calculated	Observed	Calculated
ν_1 (A_1)	250 p	250	150 p	152	111 p	114
ν_2 (E)	94 dp	92	50 dp	52	40 dp	38
ν_3 (F_2)	325 dp	325	282 dp	282	263 dp	262
ν_4 (F_2)	130 dp	132	83 dp	79	59 dp	59

^a p = polarized, dp = depolarized.

Table II-3. Force Constants and Bond Orders for MgX_4^{2-} (X = Cl, Br, and I)

Complex	Force Constants, ^a millidynes/Å			d, Å	χ_{Mg}	χ_{X}	N, Bond Order
	K	H	F				
MgCl_4^{2-}	0.669	0	0.158	2.35	1.2	3.0	0.55
MgBr_4^{2-}	0.629	0	0.113	2.50	1.2	2.8	0.52
MgI_4^{2-}	0.584	0	0.095	2.69	1.2	2.4	0.54

^a Urey-Bradley Force Constants:
 K = Mg-X bond stretching constant.
 H = X-Mg-X bond bending constant.
 F = X....X repulsion constant.

constant, f_r , for each MgX_4^{2-} species was determined. The following empirical equation derived by Gordy⁴⁴

$$N = 0.6 (f_r - 0.3) \left(\frac{d_2}{X_{Mg} X_X} \right)^{3/4} \quad (3)$$

where d is the Mg-X bond distance in Å and X_{Mg} and X_X are the electronegativities of the bonded atoms, was then used to compute the bond order, N , for the Mg-Cl, Mg-Br, and Mg-I bonds. The values of d (sum of the covalent radii), X_{Mg} and X_X , used in this calculation, are given in Table II-3 along with the computed values of N .

The observation of four Raman-active bands (one polarized and three depolarized) is consistent with the existence of a tetrahedral MgX_4^{2-} species in each of the magnesium halide systems studied. The excellent agreement between observed and calculated frequencies obtained with the simplified Urey-Bradley force field adds support to the conclusion of this study (and an earlier one⁴⁵) that these species are indeed tetrahedral. For tetrahedrally coordinated Mg(II) ions, one would expect bond orders of around 1/2, which is in good accord with the calculated values in Table II-3.

The existence of complex ions in PbX_2 -KX melts ($X = Cl$ and Br) has been investigated by Raman spectroscopy using the MG-52 ion laser for excitation. Attempts to study these systems using the He-Ne laser were relatively unsuccessful due to the much poorer signal-to-noise ratios that resulted from use of the 6328 Å line. Much better defined spectra were obtained when the 5682 Å line of the MG-52 laser was used for excitation.

The results of a previous Raman study of $PbCl_2$ -KCl melts by Balasubrahmanyam and Nanis⁴⁶ were interpreted by them in terms of the existence of a pyramidal $PbCl_3^{1-}$ species for Cl^{1-}/Pb^{2+} mole ratios from 2.5 to 3.0, and $PbCl_4^{2-}$ with distorted tetrahedral geometry for $Cl^{1-}/Pb^{2+} = 4.0$. Their interpretation was based on the reported observation of four Raman bands for melts containing 67 and 50 mol % $PbCl_2$ in KCl and nine Raman bands for a melt containing 33 mol % $PbCl_2$ in KCl.

We observed no Raman bands for pure molten $PbCl_2$, in agreement with the results of Balasubrahmanyam and Nanis. When additions of KCl were made to the $PbCl_2$ melts, a single polarized band was observed in the region from 200 to 240 cm^{-1} . This band, centered near 218 cm^{-1} , appeared to increase in intensity as the Cl^{1-}/Pb^{2+} mole ratio was increased from 2.3 to 4.0. This behavior is illustrated in Fig. II-10. No other bands were detected in the spectra of any $PbCl_2$ -KCl melts in scans from 70 cm^{-1} to 700 cm^{-1} . Scans of the region from 200 to 240 cm^{-1} with reduced slit

⁴⁴ W. Gordy, J. Chem. Phys. 14, 305 (1946).

⁴⁵ V. A. Maroni, E. J. Hathaway, and E. J. Cairns, J. Phys. Chem. 75, 155 (1971).

⁴⁶ K. Balasubrahmanyam and L. Nanis, J. Chem. Phys. 40, 2657 (1964).

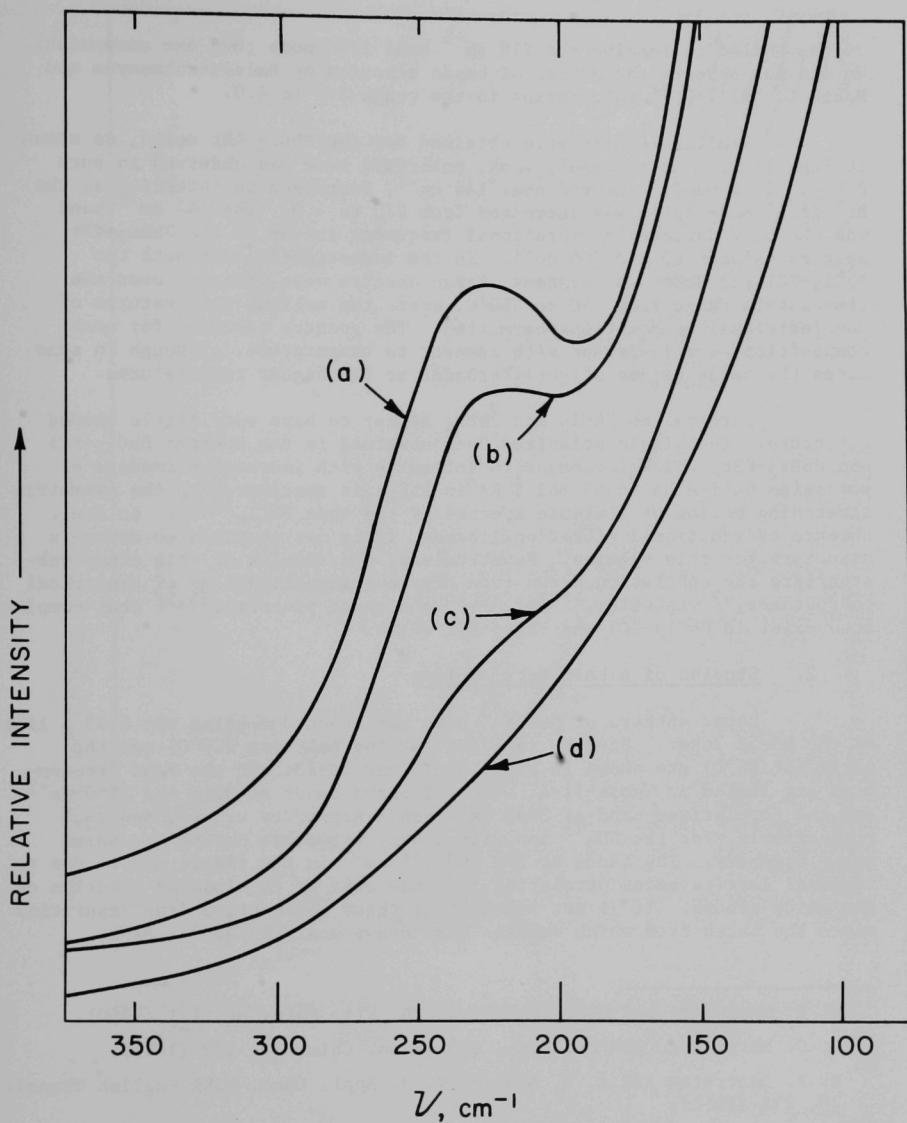


Fig. II-10. Raman Spectra of PbCl_2 -KCl Melts: (a) 33 Mol % PbCl_2 in KCl at 590°C , (b) 50 Mol % PbCl_2 in KCl at 520°C , (c) 75 Mol % PbCl_2 in KCl at 520°C , (d) Pure Molten PbCl_2 at 520°C

widths failed to resolve the 218 cm^{-1} band into more than one component. We did not observe the series of bands reported by Balasubrahmanyam and Nanis for $\text{Cl}^{-}/\text{Pb}^{2+}$ mole ratios in the range 2.5 to 4.0.

Similar results were obtained for the $\text{PbBr}_2\text{-KBr}$ melts, as shown in Fig. II-11. An extremely weak, polarized band was observed in pure PbBr_2 . This band, centered near 144 cm^{-1} , increased in intensity as the $\text{Br}^{-}/\text{Pb}^{2+}$ mole ratio was increased from 2.0 to 4.0. The 144 cm^{-1} band was the only detectable vibrational frequency in any of the $\text{PbBr}_2\text{-KBr}$ spectra between 60 and 700 cm^{-1} . In the investigations of both the $\text{PbCl}_2\text{-KCl}$ and $\text{PbBr}_2\text{-KBr}$ systems, Raman spectra were recorded over the temperature range from 390 to 590°C , where the melting temperatures of the individual compositions permitted. The spectra recorded for each composition were invariant with respect to temperature, although in some cases the bands became slightly broader at the higher temperatures.

Pure molten PbCl_2 and PbBr_2 appear to have very little bonded structure. The single polarized band observed in the systems $\text{PbCl}_2\text{-KCl}$ and $\text{PbBr}_2\text{-KBr}$, which increases in intensity with increasing amounts of potassium halide up to 67 mol % KX in PbX_2 , is attributed to the symmetric stretching motion of a simple species of the type $\text{PbCl}_n^{(2-n)}$. In the absence of additional vibrational bands, it is not possible to deduce a structure for this species. Nevertheless, the results of this study substantiate the conclusion drawn from previous investigations of electrical conductance,⁴⁷ viscosity,⁴⁸ emf,^{49,50} and vapor pressure,^{51,52} that complex ions exist in $\text{PbCl}_2\text{-KCl}$ and $\text{PbBr}_2\text{-KBr}$ melts.

2. Studies of Alkali Metal Amides

Raman spectra of NaNH_2 ⁵³ have been recorded using the 5145 \AA line of the MG-52 laser. Spectra recorded for the melt (at 220°C) and the solid (at 25°C) are shown in Figs. II-12 and II-13, and the band frequencies are listed in Table II-4. The polarized bands at 3218 and 1550 cm^{-1} and the depolarized band at 3267 cm^{-1} are assigned to ν_1 , ν_2 , and ν_3 , respectively, for the NH_2^{-} ion with a bent structure having C_{2v} point group symmetry. The bands at 500 and 225 cm^{-1} in the liquid may be due to residual lattice modes persisting into the melt or to hindered rotation of the amide groups. It is not likely that these bands arise from impurities since the batch from which samples were drawn analyzed at 96% NaNH_2 .

- ⁴⁷ M. F. Lantratov and O. F. Moiseeva, Zh. Fiz. Khim. 34, 171 (1960).
- ⁴⁸ I. G. Murgulescu and St. Zuca, Rev. Roum. Chim. 10, 129 (1965).
- ⁴⁹ M. F. Lantratov and A. F. Alabyshev, J. Appl. Chem. USSR English Transl. 26, 235 (1953).
- ⁵⁰ H. Bloom and A. J. Easteal, Aust. J. Chem. 18, 2039 (1965).
- ⁵¹ J. L. Barton and H. Bloom, Trans. Faraday Soc. 55, 1792 (1959).
- ⁵² H. Bloom and J. W. Hastie, Aust. J. Chem. 21, 583 (1968).
- ⁵³ NaNH_2 samples were prepared and analyzed by John Allen of the Chemistry of Liquid Metals Group.

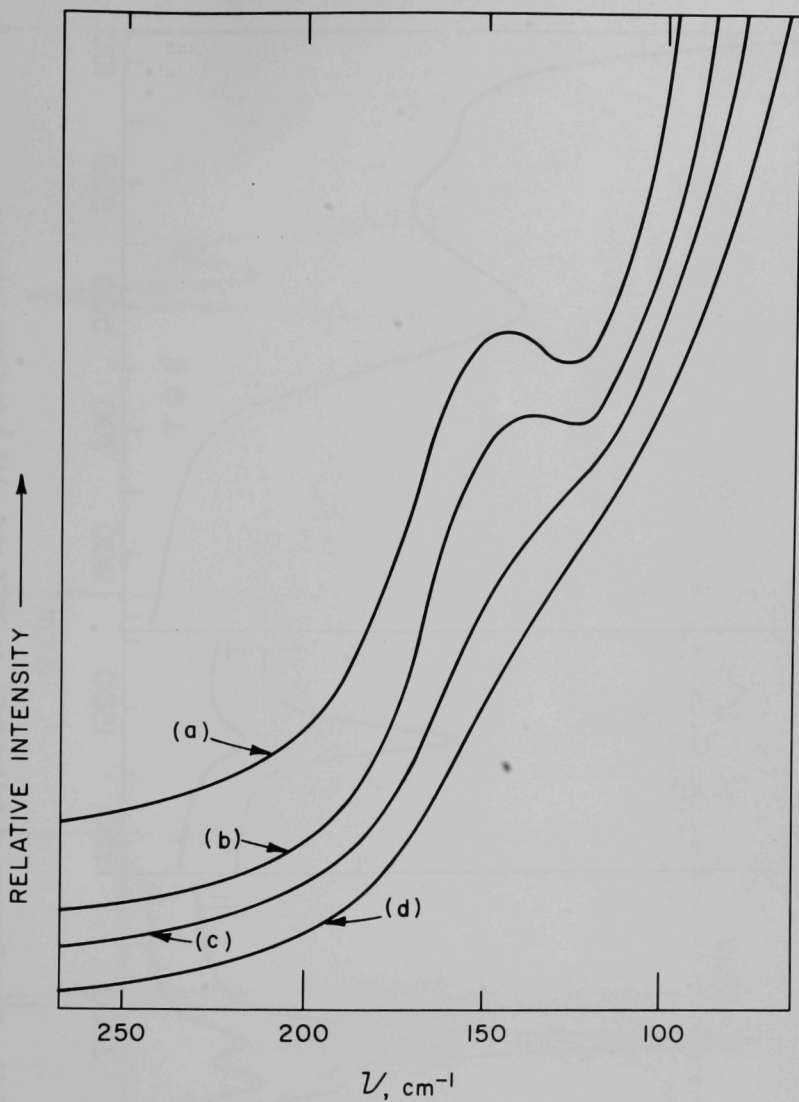


Fig. II-11. Raman Spectra of PbBr_2 -KBr Melts: (a) 33 Mol % PbBr_2 in KBr at 560°C , (b) 50 Mol % PbBr_2 in KBr at 520°C , (c) 85 Mol % PbBr_2 in KBr at 520°C , (d) Pure PbBr_2 at 520°C

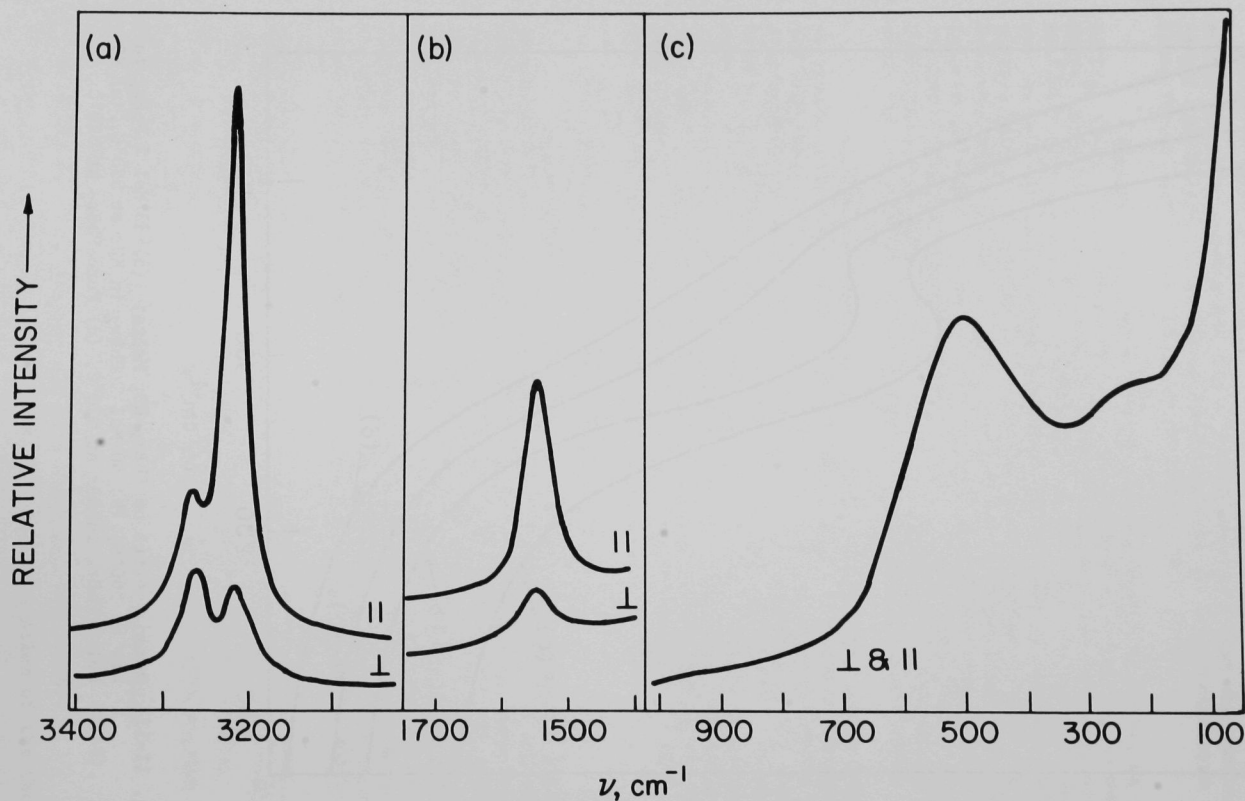


Fig. II-12. Raman Spectrum of Molten NaNH_2 at 220°C with 5145 \AA Exciting Radiation;
 (a) Sensitivity = 10^{-8} A , (b) Sensitivity = 10^{-9} A , (c) Sensitivity = 10^{-8} A ;
 || = Parallel Polarization, \perp = Perpendicular Polarization

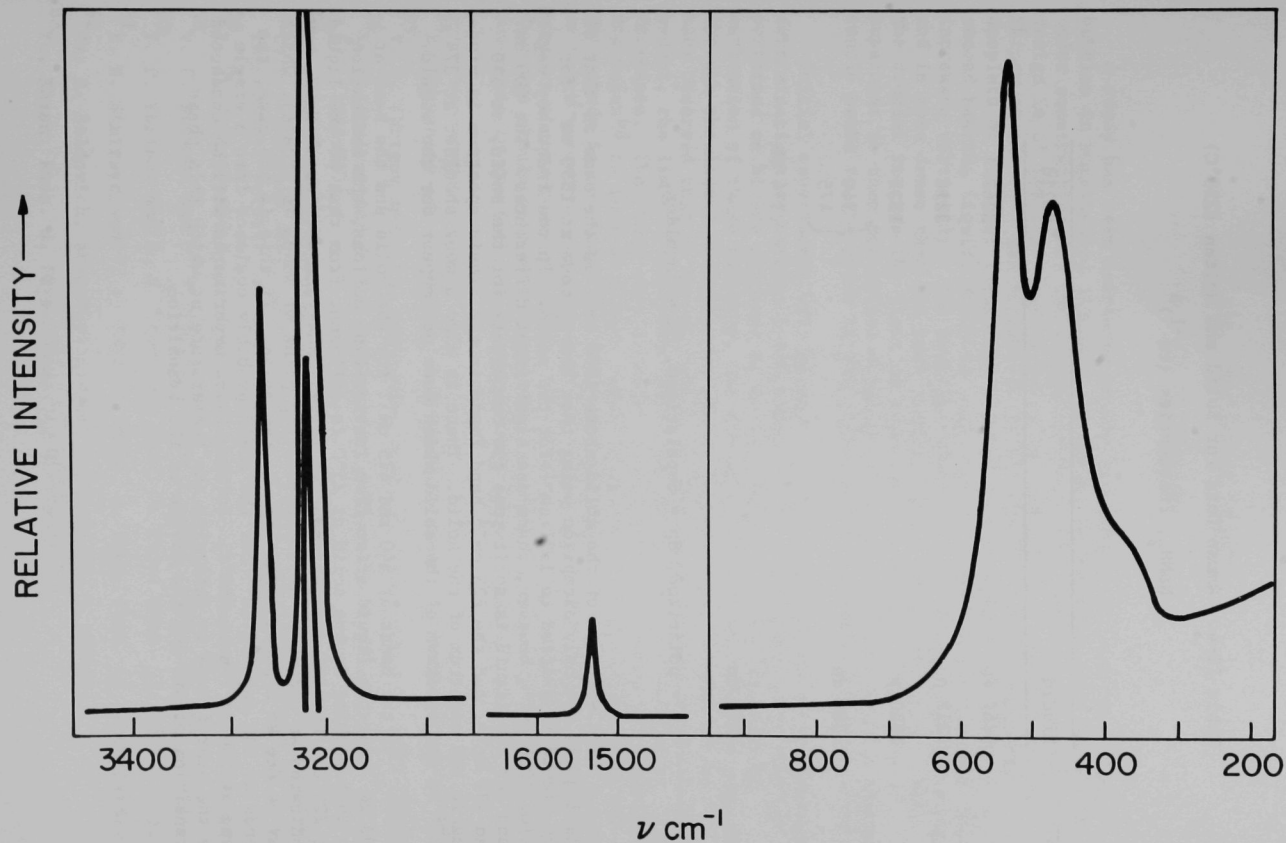


Fig. II-13. Raman Spectrum of Solid NaNH_2 at 25°C with 5145 \AA Exciting Radiation; Sensitivity = 10^{-9} A

Table II-4. Raman Data for Solid and Molten (220°C)
 NaNH_2 , Frequencies (cm^{-1})^a

Liquid	Solid
3267 dp	3267
3218 p	3218
1550 p	1531
500 dp	{ 540 475
-	~374 Sh
225 dp	-

^a p = polarized, dp = depolarized, Sh = shoulder.

The spectrum of the solid above 1000 cm^{-1} is the same as that of the liquid, the only exception being that the ν_2 mode at 1550 cm^{-1} for the liquid is shifted to 1531 cm^{-1} for the solid. In the frequency region below 1000 cm^{-1} , however, there are significant differences. The 500 cm^{-1} band for the liquid is split into two components for the solid, at 540 and 475 cm^{-1} , and the 225 cm^{-1} band found in the liquid spectrum is missing in the spectrum of the solid. There is also a weak shoulder at 374 cm^{-1} in the spectrum of the solid which does not appear for the liquid.

If the bands at 540 and 475 cm^{-1} for the solid and the band at 500 cm^{-1} for the liquid arise from lattice-type motions, the indication is that packing in the solid at 25°C is different from that of the liquid at 220°C . Preliminary differential thermal analysis studies of NaNH_2 have indicated an endotherm at 160°C (melting point of NaNH_2 is $\sim 208^\circ\text{C}$), which may be due to a phase transition in the solid. If this is the case, the bands at 540 and 475 cm^{-1} for the solid probably coalesce into a single band at 500 cm^{-1} near 160°C . Further Raman experiments will be conducted in the near future to determine the temperature at which this phase transition occurs and the nature of the transition.

III. NUCLEATION STUDIES

(J. G. Eberhart)

A study has been initiated of the homogeneous nucleation of vapor bubbles in superheated liquids. An apparatus has been designed and is under construction for the determination of the limit of superheat. The design is of the type used by Wakeshima and Takata,⁵⁴ as modified by Skipov et al.^{55,56} and Blander et al.⁵⁷ In this type of apparatus droplets of the test liquid are allowed to rise through a column of a second heating liquid, which is subjected to a temperature gradient that increases vertically. The heating liquid boils at a higher temperature and is more dense than the test liquid, and is immiscible in it. When the droplet reaches the limit of superheat, it bursts. The limit of superheat is then determined directly by moving the junction of a thermocouple probe to the point in the column where the vaporization occurred.

Initial experiments will attempt to reproduce some existing superheat determinations on various hydrocarbons.⁵⁴⁻⁶¹ Experiments will then be performed on binary mixtures of normal alkanes. In the homogeneous nucleation of these mixtures, the diffusion of the more volatile component through the liquid and into the bubble is important. Blander et al.⁵⁷ have observed that as the mixture is diluted with the less volatile component, the limit of superheat increases and the rate of nucleation decreases. They have also extended the nucleation theories of Zeldovich and Kagan⁶³ to include binary liquid mixtures. One of the purposes of this study is to extend the concentration range and the variety of systems on which superheat measurements have been made^{55,57} in order to test the mixture theory quantitatively. This extension of nucleation theory to mixtures should make the theory more useful in dealing with nucleation phenomena in reactors, such as fission product release.

⁵⁴H. Wakeshima and K. Takata, J. Phys. Soc. Japan 13, 1398 (1958).

⁵⁵V. P. Skripov and V. I. Kukushkin, Russ. J. Phys. Chem. 35, 1393 (1961).

⁵⁶V. P. Skripov and E. N. Sinitsyn, Sov. Phys. Usp. English Transl. 7, 887 (1964-65).

⁵⁷M. Blander and D. Hengstenberg, Science Center, North American Rockwell Corp., Thousand Oaks, Calif., and J. L. Katz, Clarkson College of Technology, Potsdam, N. Y., submitted to J. Phys. Chem.

⁵⁸V. P. Skripov and G. B. Ermakov, Russ. J. Phys. Chem. 37, 1047 (1963).

⁵⁹V. P. Skripov and G. V. Ermakov, Russ. J. Phys. Chem. 38, 208 (1964).

⁶⁰V. P. Skripov and E. N. Sinitsyn, Russ. J. Phys. Chem. 42, 167 (1968).

⁶¹E. N. Sinitsyn and V. P. Skripov, Russ. J. Phys. Chem. 42, 440 (1968).

⁶²Ya. B. Zeldovich, Acta Physicochim. U.R.S.S. 18, 1 (1943).

⁶³Yu. Kagan, Russ. J. Phys. Chem. 34, 42 (1960).

The surface tension is a key parameter in the theoretical expressions^{57,62,63} for calculating the rate of nucleation or the limit of superheat. The surface tensions of a few binary normal alkane mixtures⁶⁴⁻⁶⁶ have been measured, but not at the elevated temperatures required for superheat measurement and not for all the systems that might be of interest for this study. It was decided to seek a technique for estimating the surface tension of these mixtures in preference to a program of surface-tension measurement. Such a method has been devised and is described here.

Aveyard⁶⁵ and Schmidt⁶⁷ have pointed out that the surface tension of normal alkane mixtures is well represented by an empirical mixing rule proposed by Eberhart⁶⁸ of the form

$$\gamma = (Sx_1\gamma_1^\circ + x_2\gamma_2^\circ)/(Sx_1 + x_2) \quad (1)$$

where γ_i° is the surface tension of the pure i th component, x_i is the mole fraction of the i th component in the mixture, S is a constant at a given temperature, and $i = 1$ and 2 . Normal alkane mixtures display a positive deviation from linearity in γ versus x_2 , and thus $S < 1$ when $\gamma_1^\circ < \gamma_2^\circ$. Aveyard⁶⁵ has tabulated S values for seven different normal alkane mixtures at 20°C. Figure III-1 shows that S correlates well with the parameter $\theta = (\gamma_2^\circ - \gamma_1^\circ)/(\gamma_2^\circ + \gamma_1^\circ)$. The curve passes through the point (0,1) because when $\theta = 0$ the two components are identical, and thus $S = 1$ since there is no deviation from linearity in γ versus x_2 . The curve in Fig. III-1 is obtained from a regression analysis of

$$S = 1 - A\theta - C\theta^3 \quad (2)$$

which yields $A = 1.07 \pm 0.02$ and $C = 8.5 \pm 0.8$. This relationship provides the S values necessary for estimating the surface tension of normal alkane mixtures at 20°C. Convenient compilations of the surface tension of pure normal alkanes as a function of temperature are available⁶⁹ which provide γ_1° and γ_2° for Eqs. 1 and 2.

⁶⁴J. Koefoed and J. V. Villadsen, Acta Chem. Scand. 12, 1124 (1958).

⁶⁵R. Aveyard, Trans. Faraday Soc. 63, 2778 (1967).

⁶⁶R. L. Schmidt and H. L. Clever, J. Colloid Interface Sci. 26, 19 (1968).

⁶⁷R. L. Schmidt, J. Phys. Chem. 71, 1152 (1967).

⁶⁸J. G. Eberhart, J. Phys. Chem. 70, 1183 (1966).

⁶⁹"Selected Values of Physical and Thermodynamic Properties of Hydrocarbons and Related Compounds," Vol. 2, American Petroleum Institute Research Project 44, Thermodynamics Research Center, Texas A & M University, College Station, Texas (1954).

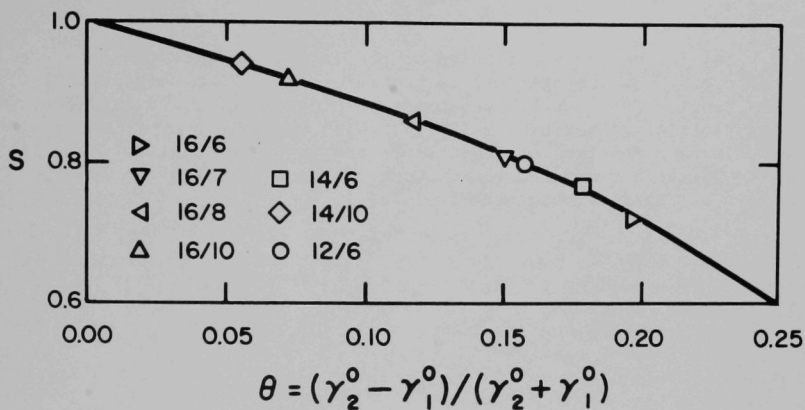


Fig. III-1. Relationship Between Mixture Parameter S and Surface Tension of Pure Components for Normal Alkane Mixtures at 20°C; Key for Experimental Points Indicates Number of Carbon Atoms per Molecule in Each Component

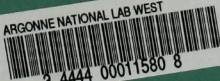
The determination of S by Schmidt⁶⁹ for the mixture of normal alkanes containing 12 and 6 carbon atoms per molecule (12/6 mixture) over the temperature range 25 to 40°C suggests that S may be constant over a sufficiently wide temperature range to be useful for estimation purposes. Thus in Eq. 1, a useful approximation is to ascribe all the temperature dependence of γ to γ_i° . The temperature dependence of the pure normal alkanes is

$$\gamma_i^\circ = \gamma_i^\circ(0)[1 - (T/T_c)]^\mu \quad (3)$$

where $\gamma_i^\circ(0)$ is the surface tension at absolute zero, T is the absolute temperature, T_c is the critical temperature, and μ is a constant. Thus surface tension data can be conveniently interpolated or extrapolated with log-log plots of γ_i° versus $1 - (T/T_c)$. With the values of γ_1° and γ_2° thus obtainable as a function of temperature and values of S at 20°C available from Eq. 2, the surface tension of normal alkane mixtures can also be estimated at other temperatures from Eq. 1.

X

ARGONNE NATIONAL LAB WEST



3 4444 00011580 8

